

# Multiscale multiphysics data-informed modeling for three-dimensional ocean acoustic simulation and prediction

Timothy F. Duda,<sup>1</sup> Ying-Tsong Lin,<sup>1</sup> Arthur E. Newhall,<sup>1</sup> Karl R. Helfrich,<sup>1</sup> James F. Lynch,<sup>1</sup> Weifeng Gordon Zhang,<sup>1</sup> Pierre F. J. Lermusiaux,<sup>2</sup> and John Wilkin<sup>3</sup>

<sup>1</sup>*Woods Hole Oceanographic Institution, Woods Hole, Massachusetts 02559, USA*

<sup>2</sup>*Department of Mechanical Engineering, Massachusetts Institute of Technology, 77 Massachusetts Avenue, Cambridge, Massachusetts 02139, USA*

<sup>3</sup>*Department of Marine and Coastal Sciences, Rutgers University, New Brunswick, New Jersey 08901, USA*

(Received 8 January 2019; revised 26 June 2019; accepted 28 June 2019; published online 1 October 2019)

Three-dimensional (3D) underwater sound field computations have been used for a few decades to understand sound propagation effects above sloped seabeds and in areas with strong 3D temperature and salinity variations. For an approximate simulation of effects in nature, the necessary 3D sound-speed field can be made from snapshots of temperature and salinity from an operational data-driven regional ocean model. However, these models invariably have resolution constraints and physics approximations that exclude features that can have strong effects on acoustics, example features being strong submesoscale fronts and nonhydrostatic nonlinear internal waves (NNIW). Here, work to predict NNIW fields to improve 3D acoustic forecasts using an NNIW model nested in a tide-inclusive data-assimilating regional model is reported. The work was initiated under the Integrated Ocean Dynamics and Acoustics project. The project investigated ocean dynamical processes that affect important details of sound-propagation, with a focus on those with strong intermittency (high kurtosis) that are challenging to predict deterministically. Strong internal tides and NNIW are two such phenomena, with the former being precursors to NNIW, often feeding energy to them. Successful aspects of the modeling are reported along with weaknesses and unresolved issues identified in the course of the work. © 2019 Acoustical Society of America.

<https://doi.org/10.1121/1.5126012>

[JAC]

Pages: 1996–2015

## I. INTRODUCTION

The propagation of sound in the sea is often complex in the sense that intricate spatial and temporal variations of energy and energy flux can arise due to heterogeneous sound speed, interaction with a structured seabed, and the motion of the heterogeneous water. In particular, acoustic propagation in shallow areas of the ocean can exhibit strong temporal and spatial variability because the properties of the water column and the bathymetry often have strong gradients. Because of this complexity, simulation of sound propagation is a commonly used tool for examining the effects (Jensen *et al.*, 2011). To represent oceanic conditions, simulations can use sound-speed fields from volumetric ocean models that follow the dynamical rules (i.e., conservation of momentum, conservation of mass, and advection/diffusion of scalar properties). The ocean models can be observationally constrained to move their state toward nature (e.g., Robinson and Lermusiaux, 2004; Moore *et al.*, 2011; Moore *et al.*, 2019), or they can run without data to simulate conditions that are dynamically possible but not matching conditions at any specific time. Simulations can also involve idealized conditions like analytically shaped seabed features, rectilinear or meandering current jets, a single tidal constituent, and so on. What is lacking at this time is a procedure to rapidly simulate three-dimensional (3D) acoustically-relevant non-hydrostatic nonlinear internal waves (NNIW) that exhibit higher acoustic property gradients than other features, and

thus have strong acoustic effects, but which are difficult to predict. Here, we describe a numerical simulation method that allows data constraints to be implemented in a manner often used in regional oceanographic mesoscale simulation and prediction, then inserts NNIWs that are consistent with the data-informed model fields, then builds 3D sound-speed fields for 3D acoustic simulations, enabling study of important acoustic effects of NNIWs.

Generally speaking, aside from the long-recognized effects on sound of seafloor shape, seabed structure, entrained air bubbles, and ice cover, there are three technical hurdles to obtaining complete simulation of sound in the sea: (i) enumerating the state of the time-dependent and spatially-varying ocean, (ii) handling the large dynamic range of the scales of ocean variability, and (iii) handling the fact that the water and sea surface are moving. In virtually all studies so far, the fluid is approximated as motionless (i.e., the low Mach number of the flow is set to zero), decoupling the particle motion of the acoustic pressure wave from the water velocity; this approximation is also used here, so number three is not addressed. A notable exception to the motionless approximation is simulation of sound reflecting from moving boundaries, for example the water surface (Siderius and Porter, 2008). Addressing the other hurdles is the topic of this paper, namely, the accurate generation of data-informed temporal snapshots of ocean condition for 3D acoustic study and prediction in shallow water, and how to compute useable ocean fields in the working area

that include all relevant scales of variability, from tens of meters in the horizontal to the mesoscale feature size of roughly 100 km.

Many papers have shown that NNIWs on continental shelves have strong acoustic effects. Propagation along the wave crests leads to strong refraction (e.g., Katsnelson and Pereselkov, 2000; Badiyev *et al.*, 2005; Collis *et al.*, 2008; Lin *et al.*, 2009; Duda *et al.*, 2012). Propagation normal to crests gives strong mode coupling that can be examined as a deterministic process (Zhou *et al.*, 1991; Preisig and Duda, 1997; Duda and Preisig, 1999; Duda, 2004) or as a stochastic process (Raghukumar and Colosi, 2014a,b). In fact, refraction and coupling can coexist (Shmelev *et al.*, 2014). The effects of NNIW crest curvature, a common NNIW characteristic, have also been examined (Lynch *et al.*, 2010; Duda *et al.*, 2011; Lin *et al.*, 2013b). The effects are strong where NNIWs are present, with Duda *et al.* (2011) presenting a formula for the NNIW amplitude required to induce significant effects 3D, but NNIWs are intermittent and often appear in groups separated by areas of considerably weaker wave activity, so the effects on acoustics will also be intermittent.

A framework to predict intermittent NNIW, and thus the intermittent acoustic effects they cause, is described in this paper. A key capability is to predict where and when NNIW packets occur, what direction they are going, and at what speed. Secondary would be prediction of NNIW wave amplitudes and other parameters, but details of nonlinear phenomena are known to be difficult to predict, so predictions of them would be relatively unreliable in comparison to the macroscopic wave packet properties. The framework consists of a sequential set of operations that result in an acoustic field prediction capability for a given location and time. Briefly, the output of a regional ocean model that includes long-wavelength internal waves and tides, but does not include short-wavelength waves which can have nonhydrostatic pressure, is used to build a field of small-scale waves that is added in to make a more inclusive 3D ocean state prediction, which is in turn passed to a 3D acoustic propagation

simulator. When ocean data are available, data-driven ocean modeling (Robinson *et al.*, 1998; Lermusiaux *et al.*, 2006; Lermusiaux *et al.*, 2010; Edwards *et al.*, 2015; Wilkin *et al.*, 2011) anchors the output to what is known about the ocean state. When they are unavailable, the framework can still be employed using idealized environmental conditions. We call the framework the Integrated Ocean Dynamics and Acoustics composite model (Duda *et al.*, 2014a; Duda *et al.*, 2014b). The first version of the entire composite model, denoted as the IODA-A model, is presented here.

The six families of operations in the composite model framework are each examined in sequence, shaping the structure of the paper. These are shown in flowchart format in Fig. 1, described as follows: (1) A regional model with surface tides and internal tides is the starting point. Specific aspects of this type of modeling that are important for acoustics are addressed. (2) Estimation of a background state (with no internal waves) in a region of interest for modeling of internal-wave propagation is required. This required separation of internal waves from a background state suffers from entangled time and space scales. An isopycnal surface tracking method is adopted. (3) Internal tides in the regional model must be characterized. For this, internal-tide signals must be extracted from the full field of isopycnal displacements (position differences from the background state) at critical locations, and their properties tabulated to form input for internal tide and NNIW propagation analysis. In this operation, internal tide propagation trajectories are computed. (4) Next, the extended rotation-modified Korteweg-de Vries nonhydrostatic wave model (eKdVf or reKdV) is run. It is initialized and constrained by both the background state and the characterized internal tides. (5) The regional model and eKdVf fields are merged into a set of volumetric ocean state snapshots, with NNIW across-crest resolution of order 10 m and along-crest resolution of order hundreds of meters to a kilometer. (6) Finally, 3D acoustic simulations are run; the parabolic equation method is used here (Lin *et al.*, 2013a).

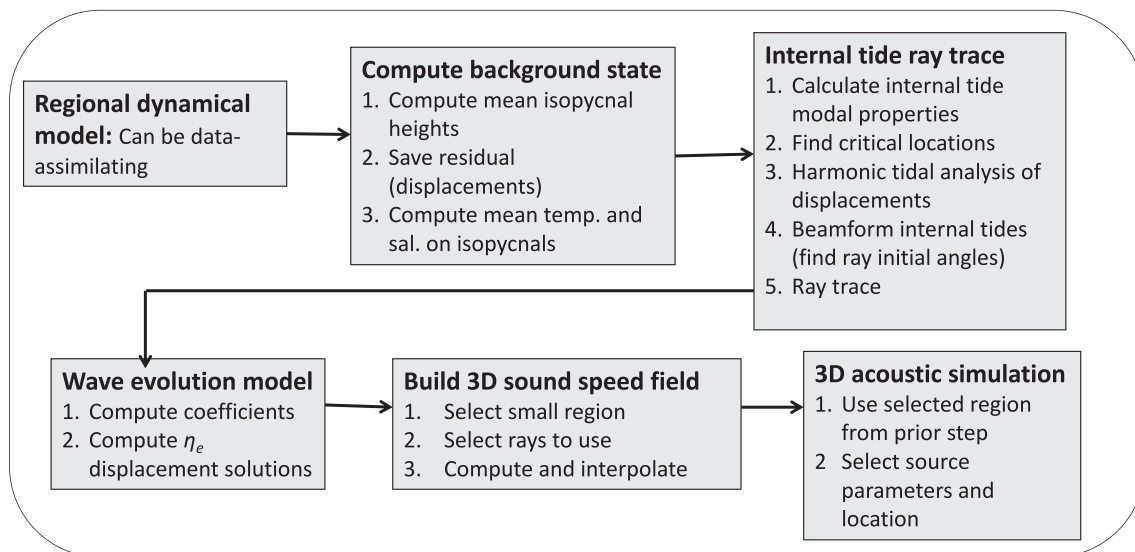


FIG. 1. Flowchart of the sequential IODA-A model operations.

The need for the sequential framework is illustrated by considering the scale of the 3D acoustic simulations shown later in this paper. Each has a scale of 3 by 6 km, and given the 1-km grid of a regional model with good resolution, there would be at most 28 model profiles in each domain. Therefore, the acoustic results would depict propagation in a gradually varying medium; depicting this in the medium having additional features of smaller scale requires insertion of statistical small-scale sound-speed anomalies (Lermusiaux, 2006), deterministic NNIW anomalies (as we do here), or theoretically generated statistically described sound-field structures from small-scale features. The sequential nature of the system invokes questions of scale separation between the fields of the various model elements. Each model element describes a specific range of scales but can also act as a bridge between scales. For example, the eKdVf model links mesoscale variability, which it does not describe to dissipation-scale activity and which it also does not describe, by showing how large scale conditions control the formation of high-shear NNIW. Scale separation is not formally treated here, but rather, the complementary capabilities and the included processes of the three main dynamical components (regional model, internal tide ray model, eKdVf tide, and NNIW model) are emphasized.

The regional modeling is covered in Sec. II. Section III describes the background state estimation. Section IV covers analysis of internal tides in the regional model. The extended rotation-modified Korteweg-de Vries modeling is explained in Sec. V. Section VI shows how the volumetric sound-speed fields are formed. The 3D acoustic simulation method is discussed in Sec. VII. Section VIII shows some example calculation results. The entire framework is examined in Sec. IX, including issues that arise when the steps are interfaced because of dynamical or other inconsistencies. Section X is a summary.

## II. REGIONAL MODELING

The first step in the modeling framework is the generation of the best available estimate of the four-dimensional ocean state. For the intended shallow-water focus of this work, contemporary state-of-the-art regional models that incorporate constraints from observations (data assimilation) and extract boundary conditions from the fields of larger-domain models are ideal to use. This use of observations to create “data driven” model fields is desirable for prediction purposes, but non-data-driven studies with idealized or archetypal conditions can also be valuable for research, so data assimilation is an option. Two families of methods are used to build the constrained model fields, including those using sequential field adjustment at the times of observations, and four-dimensional variational methods that incorporate dynamics to allow observations spaced over time to be optimally and collectively incorporated (Robinson *et al.*, 1998; Lermusiaux *et al.*, 2006; Edwards *et al.*, 2015; Wilkin *et al.*, 2011). Regional models that have been used for IODA-A purposes are the Massachusetts Institution of Technology Multidisciplinary Simulation, Estimation, and Assimilation Systems (MIT-MSEAS) primitive equation model (Haley and Lermusiaux, 2010; Haley *et al.*, 2015), the MIT General Circulation Model (MITgcm) (Marshall *et al.*, 1997), the

global Hybrid Coordinate Ocean Model (HYCOM; Bleck, 2002; Arbic *et al.*, 2010), and the Regional Ocean Modeling System (ROMS, Shechepetkin and McWilliams, 2005).

The regional modeling setup requirements to fill the needs of the IODA-A framework are (1) proper surface tides; (2) a fine enough horizontal grid to resolve internal tidal waves; and (3) a transition from an offshore region of few NNIW (or none) to a shallow-water region of plentiful NNIW. Data-assimilative 3D regional models universally use the hydrostatic pressure approximation. Models with nonhydrostatic pressure (i.e., with the full vertical equation of motion) will contain NNIW if properly set up with a very fine mesh (Venayagamoorthy and Fringer, 2006) and will not need the nested eKdVf model, but these models are seldom run in 3D because of the computational expense for resolving tidally-forced NNIWs in shallow water, with an example calculation appearing in Duda *et al.* (2016). Surface tides in the model domain can result from tidal forcing intrinsic to the model, as with global HYCOM, or they can be introduced by including tidal forcing at open boundaries (e.g., Ponte and Cornuelle, 2013).

All surface forcing options (heat, fresh water, and momentum fluxes) for the regional model are allowable in these simulations; the internal-wave modeling is agnostic toward these, but predictive simulations would benefit from adoption of the highest quality regional model fields. Options include (1) data-informed forcing with surface fluxes from weather model reanalysis, real-time products, or forecast products, (2) climatic flux conditions, or (3) no surface fluxes.

Specific modeling output fields used to date for IODA-A NNIW simulations are (1) the MSEAS Primitive Equation “Shallow Water 2006 (SW06)” product for the Middle Atlantic Bight and Gulf Stream (Haley and Lermusiaux, 2010; Kelly and Lermusiaux, 2016), (2) an idealized canyon internal tide MITgcm configuration similar to that in Zhang *et al.* (2014), but with the stratification increased from the published conditions to foster NNIW development, and (3) the ONR Inner Shelf program 200-m grid and 600-m grid ROMS configurations (Suanda *et al.*, 2017). HYCOM fields have been used only for internal tide modeling (Duda *et al.*, 2018).

Data-assimilative MSEAS output is used extensively to generate the results shown in this paper. MIT-MSEAS has already been utilized extensively for coupled ocean-acoustics predictions. Dynamical effects of the ocean environment on underwater sound propagation were forecast in real time in several ocean regions, e.g., Dabob Bay (Xu *et al.*, 2008), Mediterranean Sea (Lam *et al.*, 2009), and Middle Atlantic Bight (Colin *et al.*, 2013). In Lermusiaux *et al.* (2010), the complex tidal-to-large-scale dynamics of the northeastern Taiwan ocean region with strong internal tides and their effects of Nx2-D sound propagation were studied and successfully compared to oceanographic and acoustic transmission loss data. The results showed that with a realistic ensemble data assimilation scheme, the coupled ocean-acoustic modeling had predictive skill for both the ocean physics and acoustic fields and their uncertainties.

For the present study, MSEAS was set up for tidal-to-mesoscale dynamical studies in the Middle Atlantic Bight region, using its nonlinear free-surface hydrostatic primitive-equation model, in a configuration with generalized-level

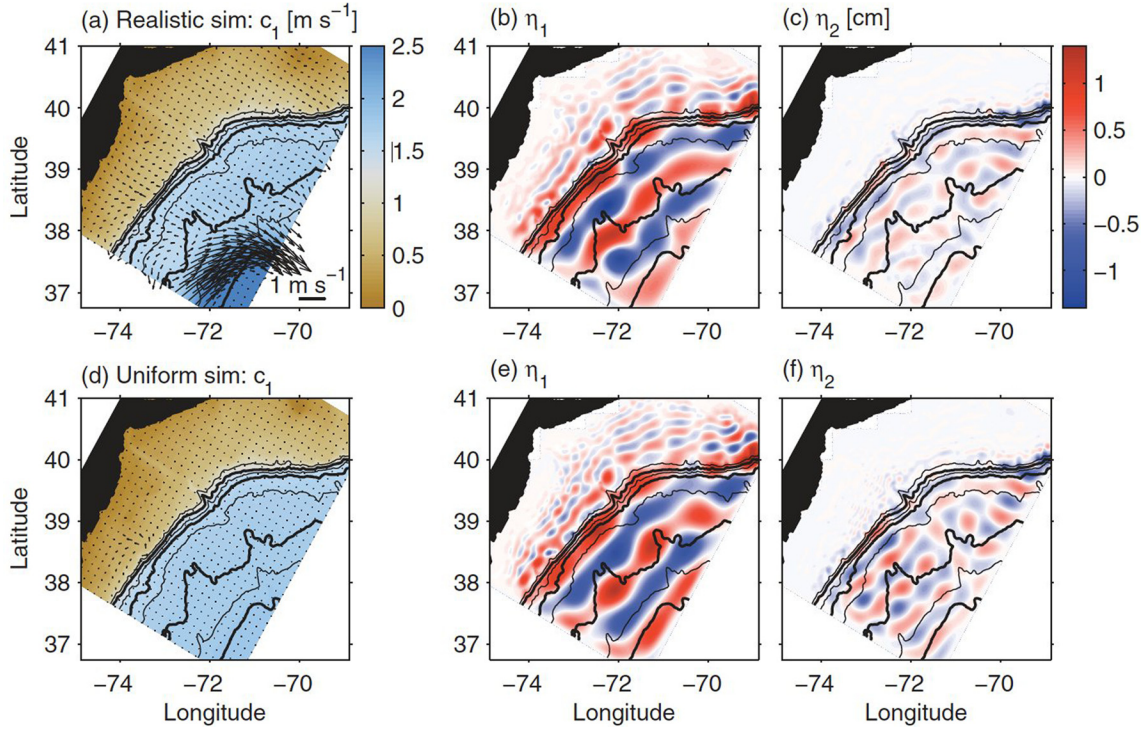


FIG. 2. (Color online) At the left are mode-one eigenspeeds and surface velocity (arrows) for (a) realistic and (d) horizontally uniform stratification simulations. Averages over a 42-day interval are shown. At the right are snapshots for the time 02:48, 1 September 2006, of the semidiurnal mode-one (the middle column) and mode-two (the third column) surface displacements from the (b and c) realistic and (e and f) uniform simulations. (Reproduced from Kelly and Lermusiaux, 2016. Note that the use here of symbols  $\eta_1$  and  $\eta_2$  conflict with their use in Section 5 onward. Here, the eigenspeed symbol  $c_1$  conflicts with our use later.)

vertical-coordinates (100 levels) and implicit two-way nested domains (1 and 3 km resolutions). Figure 2 shows the MSEAS 3-km grid domain, the long-wave eigenspeed field for mode-one baroclinic waves (similar to the speed of mode-one internal tides, see Sec. III B), and extracted amplitudes of mode-one and mode-two semidiurnal internal tides. Features to note are the slow wave speeds and shorter wavelengths in shallow water compared to deep water, the ratio of mode-two to mode-one energy in the shallow areas (much less than one), and the effect of the Gulf Stream at the south end on the wave speeds, caused by a movement of the main thermocline down towards the center of the water column. The eigenspeeds in the figure are mode-one eigenvalues of the equation for long-wave normal modes with no rotation (mode one has the highest speed and the fewest zero crossings of the vertical mode shape  $\phi$ )

$$\frac{d^2\phi(z)}{dz^2} + \frac{N^2(z)}{c^2}\phi(z) = 0, \quad (1)$$

which are useful for normal-mode decomposition of baroclinic ocean wavefields. Here,  $N$  is the buoyancy frequency,  $N = [-g(\rho^{-1}\partial\rho/\partial z)]^{1/2}$  where  $\rho$  is potential density and  $g$  is the acceleration of gravity. Figure 3 shows a surface temperature snapshot for the 1-km domain that we use for results in this paper, which is nested into the 3-km domain of Fig. 2.

To test the IODA-A system in a shelf break canyon region where the basic pattern of inhomogeneous internal wave field is known, we carried out an idealized canyon simulation using hydrostatic MITgcm. The model spans 720 and 875 km in the along- and across-shelf directions, respectively. The boundaries are periodic in the along-shelf direction and

open in the across-shelf direction. The model horizontal resolution changes from 5 km on the boundaries to 250 m in the central region of the domain. It has 170 vertical layers with grid spacing varying from 1.5 m on the surface to 40 m on the bottom. There are  $600 \times 720 \times 170$  ( $\sim 73 \times 10^6$ ) grid cells. Similar to the ROMS model in Zhang *et al.* (2014), this MITgcm model has a Gaussian-shaped canyon incising into

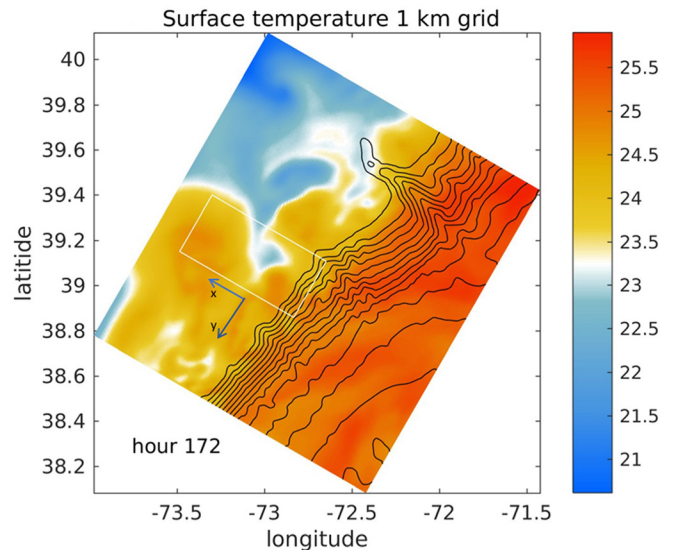


FIG. 3. (Color online) (a) Surface temperature (unit:  $^{\circ}\text{C}$ ) is shown versus latitude and longitude for the 1-km MSEAS SW06 domain, hour 172 (21 August 2006 04:00 UTC). A box for NNIW and acoustic modeling in upcoming sections is outlined, with  $x$  and  $y$  axes indicated. Depth is contoured at 400 m intervals.

the outer-shelf and is forced by  $M_2$  tides on the offshore boundary. The initial stratification of the model differs from that in Zhang *et al.* (2014) in the uppermost 85 m, where the climatological profile is replaced by a summertime profile measured on the continental shelf. A density snapshot at 30-m below surface from the MITgcm simulation [Fig. 4(a)] shows a patch of negative density anomaly  $\sim 20$  km to the right of the canyon axis (facing coast), indicating downward displaced density interface. The density anomaly patch reflects the spatial focus of the internal tides generated at the sources along the 220-m isobath contour line. Due to the canyon topography, the phases of the internal tide sources differ and cause a phased-array-like behavior of the internal tides, forming a horizontal beam of internal tide radiation, resulting in the focus of the internal tide energy (Zhang *et al.*, 2014). Because of the low resolution and the hydrostatic approximation, this simulation does not produce any NNIW. For comparison, we also carried out a 3D nonhydrostatic MITgcm simulation with the same model domain, bathymetry, and forcing, but a much higher resolution ( $\sim 25$  m in the canyon region) to examine the NNIWs. The total number of grid cells is  $1440 \times 2160 \times 170$ . This computation is exceedingly expensive: The simulation of  $6 M_2$  tidal cycles takes four weeks with 720 CPUs. This cost effectively motivates the IODA-A composite model effort. The produced density field at the same time and depth [Fig. 4(b)] shows a packet of NNIWs with wavelength of 100–500 m propagating onshore to the right of the canyon, corresponding to the patch of negative density anomaly in the hydrostatic simulation.

### III. ESTIMATION OF THE OCEAN BACKGROUND STATE

The ocean background state is the temperature, salinity, and current structure that includes features of motion at

subtidal frequencies. The background state, without tidal and internal tidal features, is needed to calculate time- and space-dependent internal wave parameters, such as mode shape and modal phase velocity, for our internal wave modeling. This section explains how the background state and the mode parameters are computed.

#### A. Separating internal waves, tides, and subtidal features

The next step after obtaining tidally-forced regional model fields is to separate the internal waves features in the model fields, including internal tides, from the background state that they propagate in. This is necessary because the eKdVf model solves for concurrent propagation, in a non-tidal background condition, of internal tides and higher frequency NNIW. A low-pass filtering procedure explained in the next paragraph is adequate to form the background stratification. Tidal band currents are removed by time averaging over an integral number of semidiurnal periods. The eKdVf will recreate a version of the removed internal tides, but advection of the waves by barotropic tidal currents is not included in results shown here. An optional initial step to later enable barotropic tidal advection of the internal waves is to compute and subtract barotropic tidal currents from the model current field using harmonic analysis, or subtract tidal current estimated from another source (the difference will be small for a properly set up model, Logutov and Lermusiaux, 2008) and correct later for their presence by advecting all water column features along tidal ellipse trajectories. This step is not taken here, so horizontal tidal displacements of order 500 m root-mean-square (rms) are absent from maps shown here.

The internal-tide isolation is implemented by finding mean isopycnal heights in moving time-windows (length

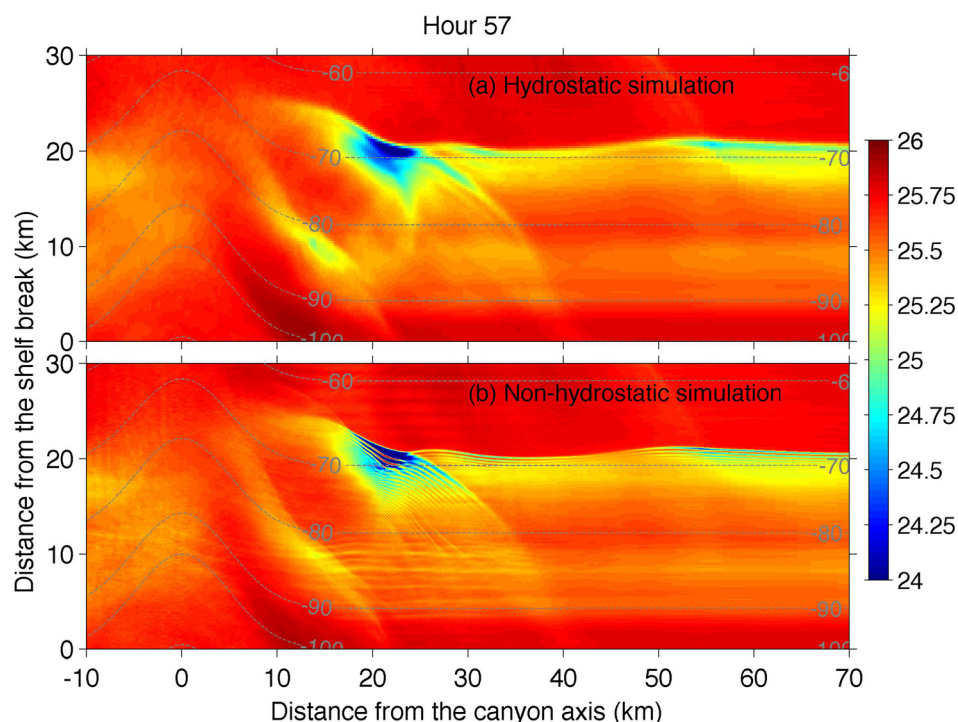


FIG. 4. (Color online) (a) A time snapshot of density at 30-m depth is shown in the vicinity of a canyon with an  $M_2$  barotropic tide incident from offshore. The blue shows a large wave of depression that is not properly modeling in this hydrostatic-pressure simulation. (b) The costly simulation with nonhydrostatic pressure, taking 480 000 CPU hours for six tidal cycles, properly simulates the NNIW. The dashed grey lines are the bathymetry contours every 10 m. Figure reproduced from Duda *et al.* (2016).

$W$ ); typically  $W = 72$  h. The heights ( $z'$ ) of isopycnals (surfaces of uniform density  $\rho$ ) on a dense vertical grid at all positions are found via interpolation from typically hourly model fields, yielding  $z'(x, y, \rho, t)$ . The time mean of this is the mean height of the isopycnals. Temperatures ( $T$ ) and salinities ( $S$ ) at these heights are then tabulated, also via interpolation, creating  $T(x, y, \rho, t)$  and  $S(x, y, \rho, t)$ . The time mean of the heights,  $T$  and  $S$  give the mean fields  $Z(x, y, \rho)$ ,  $T_\rho(x, y, \rho)$ ,  $S_\rho(x, y, \rho)$ , and the functions  $T_B[x, y, Z(\rho)]$ , and  $S_B[x, y, Z(\rho)]$ . Using these,  $T$ ,  $S$ , and  $\rho$  can be interpolated onto a set of standard depths ( $z$ ) everywhere in the model  $x$ - $y$  grid. The residual heights  $\eta = z' - Z$  are the isopycnal displacements. The inverse function of  $Z(x, y, \rho)$  is the background stratification,  $\rho_B(x, y, z)$ . Figure 5 shows results of this procedure for one specific computation. Finally, the background sound-speed  $c_B$  is computed from  $T_B$  and  $S_B$ .

The background current field is needed for internal tide and eKdVf analysis. Mean geostrophic current is computed using the thermal wind equations with a level of no motion at the seabed. A second background current estimate is

computed by simply averaging currents point-by-point over the selected time window.

## B. Computing internal tide modes

Once the background state is established, the parameters governing internal wave propagation can be computed and then passed to propagation algorithms. Two sets of parameters are needed. The first set is computed on the  $x, y$  plane and governs propagation of mode-one waves of tidal frequency (mode-one internal tides), and the second set contains the coefficients of the mode-one eKdVf. The first set is needed first and their calculation covered here, while their use to determine internal-tide behavior is covered in Sec. IV.

The internal-tide modal parameters within a water column with sheared background currents in geostrophic balance are found using the generalized Jones equation. A reduced version of this equation valid for parallel sheared geostrophic background flow was derived by Jones (1967), and the full version is examined in Duda *et al.* (2018). Written

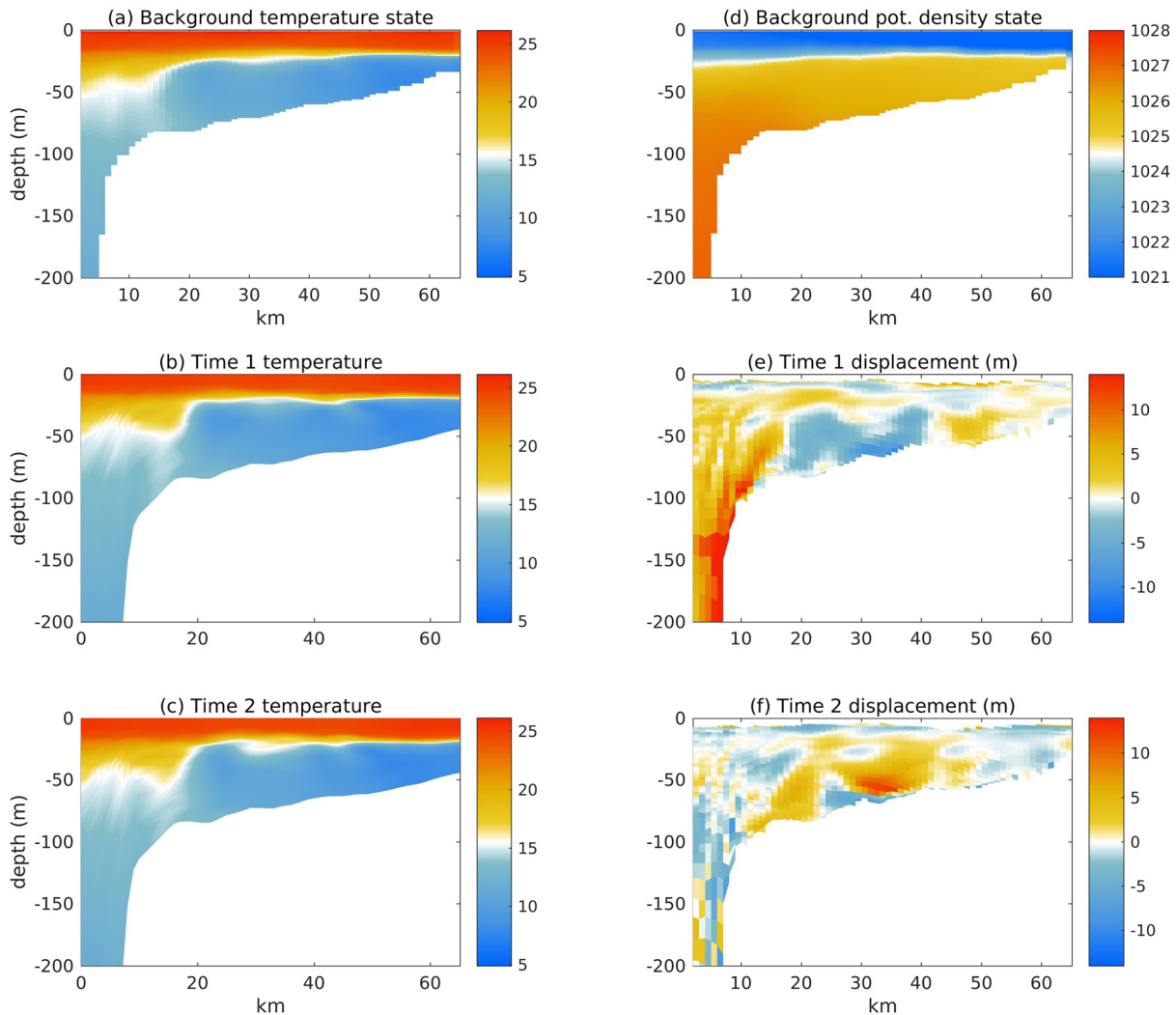


FIG. 5. (Color online) Images of fields from the MSEAS background state processing (72-h average, hour 172 start). Transects are from the centerline of the processing area box in Fig. 3. (a) The background temperature state is shown,  $T_B(x, y, z'(\rho))$ . (b) A time snapshot of temperature is shown,  $T(x, y, z', t_1)$ ,  $t_1$  is hour 188. (c) Another temperature snapshot,  $T(x, y, z', t_2)$ ,  $t_2$  is hour 194, one-half tidal cycle after  $t_1$ . (d) The background potential density state is shown,  $\rho_B(x, y, z)$ . (e) A time snapshot of computed displacement is shown,  $\eta(x, y, z', t_1)$ . (f) A second snapshot of displacement is shown,  $\eta(x, y, z', t_2)$ , 6 h after the time for panel (e).

for horizontally progressive harmonic waves of the form  $\psi(x, y, z, t) = \hat{w}(z)\exp(-i\omega t + ikx + ily)$ , the equation is

$$\begin{aligned} & \omega'(\omega'^2 - f^2)\frac{d^2\hat{w}}{dz^2} + 2\left[-f^2\left(k\frac{du_0}{dz} + l\frac{dv_0}{dz}\right) \right. \\ & \left. -i\omega'f\left(l\frac{du_0}{dz} - k\frac{dv_0}{dz}\right)\right]\frac{d\hat{w}}{dz} + \left\{\omega'(N^2 - \omega'^2)(k^2 + l^2) \right. \\ & \left. + \omega'^2\left(k\frac{d^2u_0}{dz^2} + l\frac{d^2v_0}{dz^2}\right) - i2f\left(k\frac{du_0}{dz} + l\frac{dv_0}{dz}\right) \right. \\ & \left. \times \left(l\frac{du_0}{dz} - k\frac{dv_0}{dz}\right) - i\omega'f\left(l\frac{d^2u_0}{dz^2} - k\frac{d^2v_0}{dz^2}\right)\right\}\hat{w} = 0. \end{aligned} \quad (2)$$

Here,  $f$  is the Coriolis parameter,  $\rho$  is the potential density, and  $\omega'$  is the depth-dependent intrinsic wave frequency in a Lagrangian frame following a geostrophic background current  $(u_0, v_0)$ , i.e.,  $\omega'(z) = \omega - ku_0(z) - lv_0(z)$ . Here, solutions of Eq. (2) are called the “full modes” for internal waves propagating in baroclinic currents with arbitrary stable density gradient  $N^2$ . Examination of this equation and of internal wave modes in shear flows appears in Duda *et al.* (2018). Solution of this equation with boundary conditions of zero displacement at the surface (an approximation) and at the seafloor yields the modal shapes  $\hat{w}_n(z)$  and modal wavenumbers  $k_n$  and  $l_n$ , with subscript  $n$  denoting eigenvalue index.

The full mode Eq. (2) is a fifth-order equation in wavenumber and is a polynomial eigenvalue problem. The

solution method that has been chosen is to find modal phase speed eigenvalues  $c_n(\theta)$  as a function of geographic direction. The equation is first converted to a fifth-order polynomial function of  $c(\theta) = \omega/|\mathbf{k}|$ , where  $\theta$  is the angle of the wave vector  $\mathbf{k} = (k, l)$ . In general, the set of solutions  $c_n(\theta)$  at each  $n$  is anisotropic, with fastest wave speed found in the downstream direction of the dominating current. For a given location, the  $N^2$  and current profiles  $U = [u_0(z), v_0(z)]$  need to be provided along with a selection of  $\theta$  values, yielding mode speed  $c_n$  (eigenvalue with index  $n$ ) and  $\hat{w}_n(z)$  as functions of direction. Mode one and  $c_1$  are primarily used in this paper. Figure 6 shows fields from the 1-km MSEAS model output (also in Fig. 3), which is examined throughout this paper, extracted during one calculation. The figure also shows  $c_1(x, y)$  for four internal-wave wavenumber directions  $\theta$ , all at the  $M_2$  tidal frequency. Along the southwestern boundary of the subgrid area within which  $c_1$  is computed it can be seen that waves moving to the southwest in the direction of the current [Fig. 6(e)] have significantly faster speeds than waves moving to the northeast [Fig. 6(b)].

Note the modeling procedures (1)–(6) listed in Sec. I can be completed for any area of any tide-inclusive regional model at any modeled time. This paper shows results from an idealized model of a canyon area, and from one rectangular box of the MSEAS model where the SW06 field program took place.

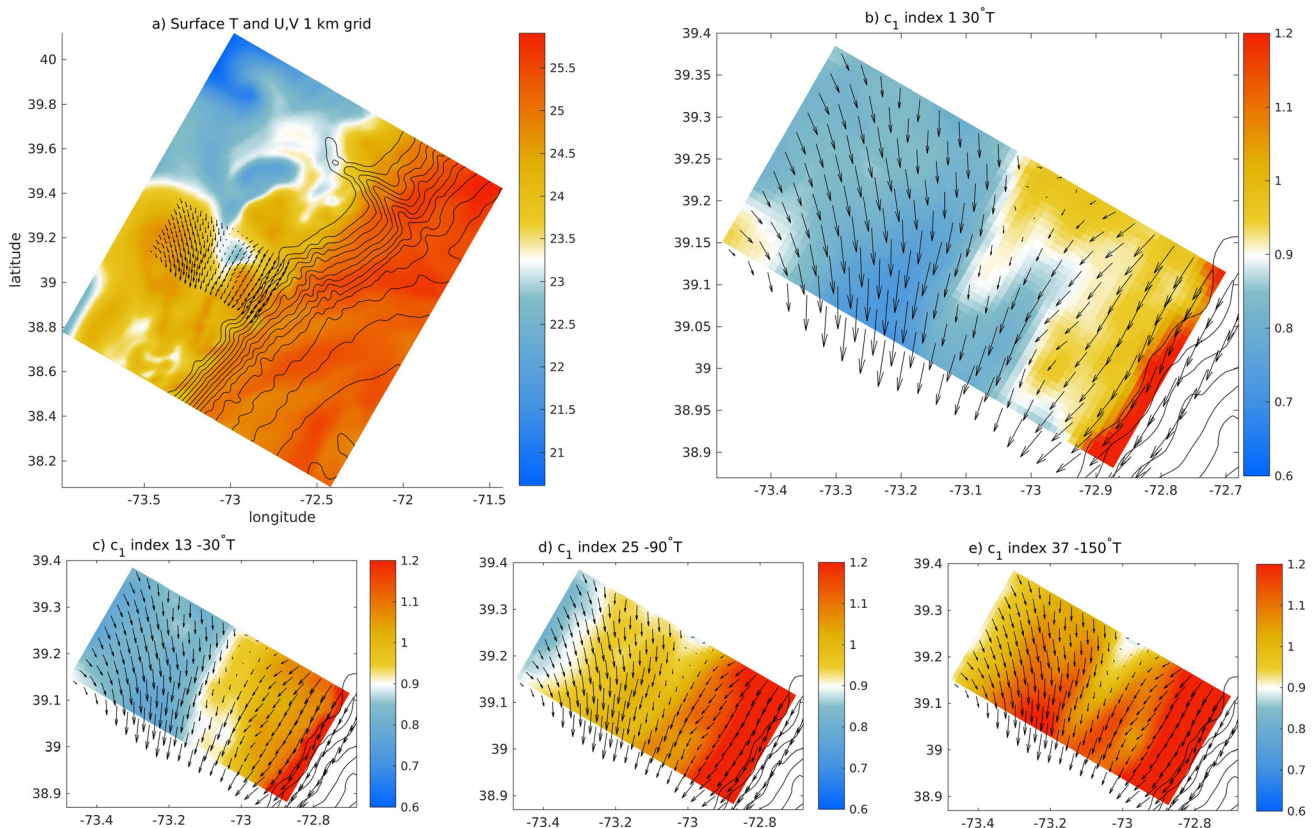


FIG. 6. (Color online) (a) The time snapshot surface temperature (color) of the model state shown in Fig. 3 is repeated with surface current arrows added. Arrows are shown at every 2nd grid point, at 2-km spacing, so that one quarter of the arrows are shown. The maximum current is 23 cm/s. Bathymetry is shown with 200-m contour interval. (b) For the same snapshot, the mode-one speed  $c_1(x, y, \theta)$  (color) from (2) is shown for  $\theta = 30^\circ$  re true north,  $M_2$  semidiurnal tidal period ( $2\pi\omega^{-1} = 12.42$  h). (c) As in (b) but for  $\theta = 330^\circ$ . (d) As in (b) but for  $\theta = 270^\circ$ . (e) As in (b) but for  $\theta = 210^\circ$ .

#### IV. EXTRACT INTERNAL TIDE AND TRACE MODAL RAYS

Tracing internal tide rays from the shelf edge area on to the shelf in the background state is one way to estimate the behavior of internal tides in the model. Tidal line filtering or band filtering of the model fields is another method (Kelly and Lermusiaux, 2016), but this does not move us directly to our goal of modeling NNIW, using the eKdVf model, that would be consistent with the model state. The behaviors of internal tides that we require are direction of propagation on the shelf, plus tidal amplitude and tidal waveform at an offshore location prior to propagation onto the shelf. The direction of propagation is found by tracing internal tide rays from offshore locations using the  $c_1(x, y, \theta)$  fields explained in Sec. III B. Ray initial directions are found by tidal analysis of the displacements  $\eta(x, y, z, t)$  estimated from the model.

This section will show the ray tracing method, methods for determining ray initiation locations, and ray initiation directions. Mode one, with a vertical displacement profile all of the same sign, will be given the majority of the attention because field studies show this to be dominant (e.g., Rippeth and Inall, 2002; Duda and Rainville, 2008).

##### A. Internal wave modal ray tracing in baroclinic currents

A complete description of a method for tracing internal wave modal rays in ocean regions having baroclinic background currents appears in Duda *et al.* (2018). The method is briefly described here. The ray equations are written in terms of the angle  $\alpha(x, y) = \arctan(p_y/p_x)$ , which is the direction of a vector normal to the phase front, with  $p_x = \partial\phi/\partial x$  and  $p_y = \partial\phi/\partial y$  being phase derivatives of the wave moving along the ray. For rays of mode-one internal waves of a defined frequency, the slowness field  $S(x, y, \alpha) = c_1^{-1}$  evaluated at the phase-normal angle is needed, as well as its derivative with respect to azimuth. Spatial variations of  $S$  will arise from  $x, y$  variations in the profiles  $N^2(z)$ ,  $u_0(z)$ , and  $v_0(z)$ . The equations to be integrated to yield ray locus  $[x(s), y(s)]$  are

$$\begin{aligned} \frac{dx}{ds} &= R \left( S(\alpha) \cos \alpha + \sin \alpha \left. \frac{\partial S}{\partial \theta} \right|_{\theta=\alpha} \right), \\ \frac{dy}{ds} &= R \left( S(\alpha) \sin \alpha - \cos \alpha \left. \frac{\partial S}{\partial \theta} \right|_{\theta=\alpha} \right), \\ \frac{dp_x}{ds} &= RS(\alpha) \frac{\partial S}{\partial x}, \\ \frac{dp_y}{ds} &= RS(\alpha) \frac{\partial S}{\partial y}, \end{aligned} \quad (3)$$

with normalization factor

$$R = \left( S^2(\alpha) + \left[ \left. \frac{\partial S}{\partial \theta} \right|_{\theta=\alpha} \right]^2 \right)^{-1/2}. \quad (4)$$

Here, the coordinates  $(x, y)$  define the ray trajectory with arclength increment  $ds$ . An auxiliary quantity is the slope  $M$  of the ray path given by

$$M = \frac{dy}{dx} = \tan \beta = \frac{S(\alpha) \sin \alpha - \cos \alpha \left. \frac{\partial S}{\partial \theta} \right|_{\theta=\alpha}}{S(\alpha) \cos \alpha + \sin \alpha \left. \frac{\partial S}{\partial \theta} \right|_{\theta=\alpha}}. \quad (5)$$

At any position on the trajectory the ray angle is  $\beta(x, y) = \arctan(M)$ . Implementing the equations requires specification of the starting phase-front normal angle  $\alpha$ . An initial  $\beta$  can be given and the consistent initial  $\alpha$  can be found by solving Eq. (5) with a standard iterative method. For the case of isotropic  $S$  (i.e.,  $\partial S/\partial \theta = 0$ ) these equations simplify to established equations. In the isotropic case  $\alpha$  equals  $\beta$  (i.e., skew angle  $\alpha - \beta = 0$ ).

##### B. Select ray starting locations

Here, the starting locations for mode-one internal tide rays moving onshore are taken to be at or near the locus of the critical bathymetric slope. The critical bathymetric slope exists when the slope passes from subcritical to supercritical, with criticality defined using the normalized bottom slope

$$\gamma = S_B/S_C, \quad (6)$$

where  $S_B$  is the bathymetric slope and  $S_C$  is the (depth-dependent) internal wave energy propagation characteristic slope satisfying

$$S_C = \tan \zeta = \left( \frac{\omega^2 - f^2}{N^2 - \omega^2} \right)^{1/2}. \quad (7)$$

Here,  $\zeta$  is the angle of the characteristics with respect to horizontal, and the stratification strength ( $N^2$ ) is evaluated close to the seabed. The slope is critical when  $\gamma$  equals one. At criticality, singular situations can occur in inviscid linear theory such as unbounded energy upon reflection, but reflection is predicted to behave better in practice (Hall *et al.*, 2013).

In many continental slope regions, the bathymetry is steep and  $\gamma > 1$  on the main slope (the slope is supercritical),  $\gamma < 1$  on the shelf (shelf is subcritical), and the locus of critical slope lies along the edge of the shelf at the top of the slope (the shelf break). Analysis of internal tide generation in such geometries by Zhang and Duda (2013) and Zhang *et al.* (2014) shows that internal tides develop at a critical shelf break above a supercritical slope, in agreement with many previous studies, including the illustrative laboratory experiment of Zhang *et al.* (2008). Furthermore, those papers quantify the energy flux as a function of position and find the maximum flux divergence to lie at the shelf break (the critical locus), with energy flux offshore in deep water and onshore in water shallower than the critical locus. In addition, good representations of internal tides on the shelf can be made by summing mode-one internal tides from point sources at the critical locus (Zhang *et al.*, 2014), further evidence that the critical area makes a good starting point for propagation of mode-one internal tides.

Because of the flux divergence at the critical locus, we set ray initial locations at or near the critical locus. This is found by evaluating Eq. (7) then Eq. (6) everywhere, using



the background  $N(z)$  (Sec. III A). In the example calculations shown here, for grid line in the along-shelf direction, the cross-shelf grid location that is immediately inshore of the supercritical to subcritical  $\gamma$  transition at the shelf edge is chosen as the critical locus. This makes a set of grid points, one point for each along-shelf grid index, denoted  $(x_C, y_C)$ . Figure 7 shows an example line of ray starting points  $(x_S, y_S)$  in relation to  $(x_C, y_C)$  for one study. The  $(x_C, y_C)$  locations can be chosen as ray starting points, but other options can be chosen at the user's discretion, for example a line in the vicinity of the critical loci. Typically, the start is adjusted inshore by 1 km because the internal tides seem better suited for analysis. It is easiest to choose ray start points that are on the model grid, where processed data are available, without interpolation, for the further analysis needed for ray starting and eKdVf initialization.

### C. Determine ray starting angles

The initial ray phase-front normal directions  $\alpha$ , or the initial trajectory angles  $\beta$ , at the starting points are found by tidal analysis of the displacements  $\eta(x_S, y_S, z, t)$  at the ray starting points. The relative phases of the internal tides at the sites determine the ray starting angles. Internal tides created at a critical shelf break are known to have bottom-concentrated energy, with the waves in the form of beams that are consistent with the energy residing in many modes (Gerkema *et al.*, 2004; Carter *et al.*, 2008; Kelly *et al.*, 2010; Zhang *et al.*, 2008; Zhang and Duda, 2013). Therefore, the wave energy near the seabed is analyzed to determine the wave propagation direction. Tidal analysis is performed in time windows equal to the background state averaging duration  $W$ , which can be overlapping if high-resolution analysis is desired. Analysis is restricted to the deepest 60% of the

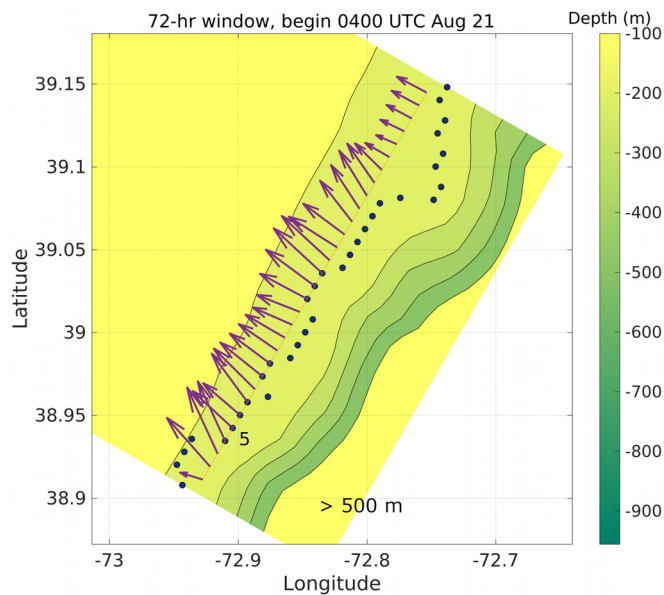


FIG. 7. (Color online) Details from a ray initialization are shown. The circles show the benchmark critical locations. The line connects the sites chosen for ray initialization, which is one point shoreward on the grid of the median cross-shelf grid index value of the critical sites. The arrows indicate the ray initial angles, with arrow lengths proportional to the variances of the analyzed tidal displacements.

water column. At each ray starting point, the displacement time series at the single depth of greatest displacement variance over the time window (typically 72 h) is processed with harmonic tidal analysis to yield the best-fit tidal signals (Pawlowicz *et al.*, 2002), called  $\eta_{IT}(x_S, y_S, t)$ . In the MSEAS-SW06 area simulations, between 10% and 35% of the analyzed displacement energy is fitted to tidal oscillations, varying from site to site. Figure 8(a) shows example displacement time series  $\eta(x_S, y_S, z, t)$  at one  $(x_S, y_S)$  ray start position. The computed displacements near the seabed in Fig. 8(a) are more clearly oscillatory and tidal than the displacements closer to the surface. In Fig. 8(b), phase shifts of the internal tidal displacements  $\eta_{IT}(x_S, y_S, t)$  computed at different ray starting positions are evident, consistent with wave crest bending, or equivalently, with variation of  $\alpha$  along the line of starting points.

Using the distances between triplets of  $(x_S, y_S)$  points (arranged along a line in the example of Fig. 7), and using the wavelength of the local internal tide with no current assumed, a correlation analysis of the tidal waveforms is used to determine the phase lag and thus the phase propagation direction. For each  $(x_S, y_S)$ , the time lag  $\Delta t$  of correlation maximum with the wave-forms to the right and left are converted to propagation distance,  $\Delta x = \omega_{M_2} \Delta t k_{M_2}^{-1}$  using the  $M_2$  semidiurnal frequency and local baroclinic mode-one wavelength, and then to  $\alpha = \tan^{-1}(\Delta x / \Delta y)$ .

### D. Compute ray trajectories

Trajectories of rays computed with Eqs. (3) and (4) in the background environment are relatively straight, despite the complexity of the current and density variations, compared to behavior of deep-water mode-one waves crossing extreme features such as the Gulf Stream (Duda *et al.*, 2018). Figure 9(c) shows one set of shelf rays, also computed for the conditions in the SW06 experiment modeled with MSEAS. The crossing of rays is governed largely by the initial angles, although adjacent rays (1-km initial spacing) do exhibit different curvatures to the extent that they

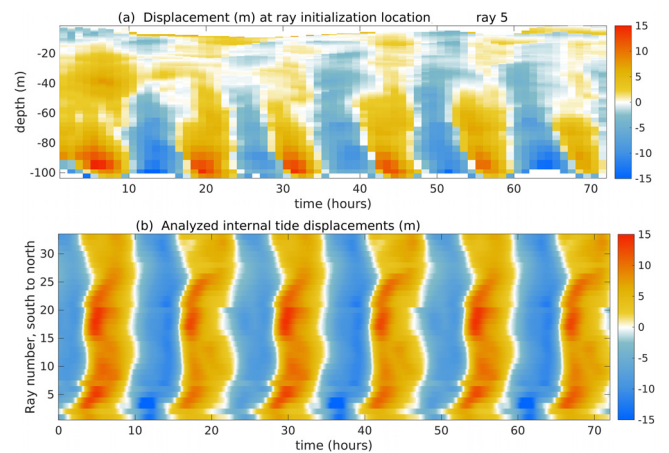


FIG. 8. (Color online) Displacements  $\eta(x_S, y_S, z, t)$  at ray starting points near the shelf break are shown. (a) Extracted displacement  $\eta(z, t)$  is shown versus depth and time for ray 5 initial location; see Fig. 7. (b) Displacement analyzed to form input to ray tracing and eKdVf solving is shown versus time and ray location; see Fig. 7. The locations are 1.0 km apart. The visible internal tide phase variations lead to initial ray angle variations.

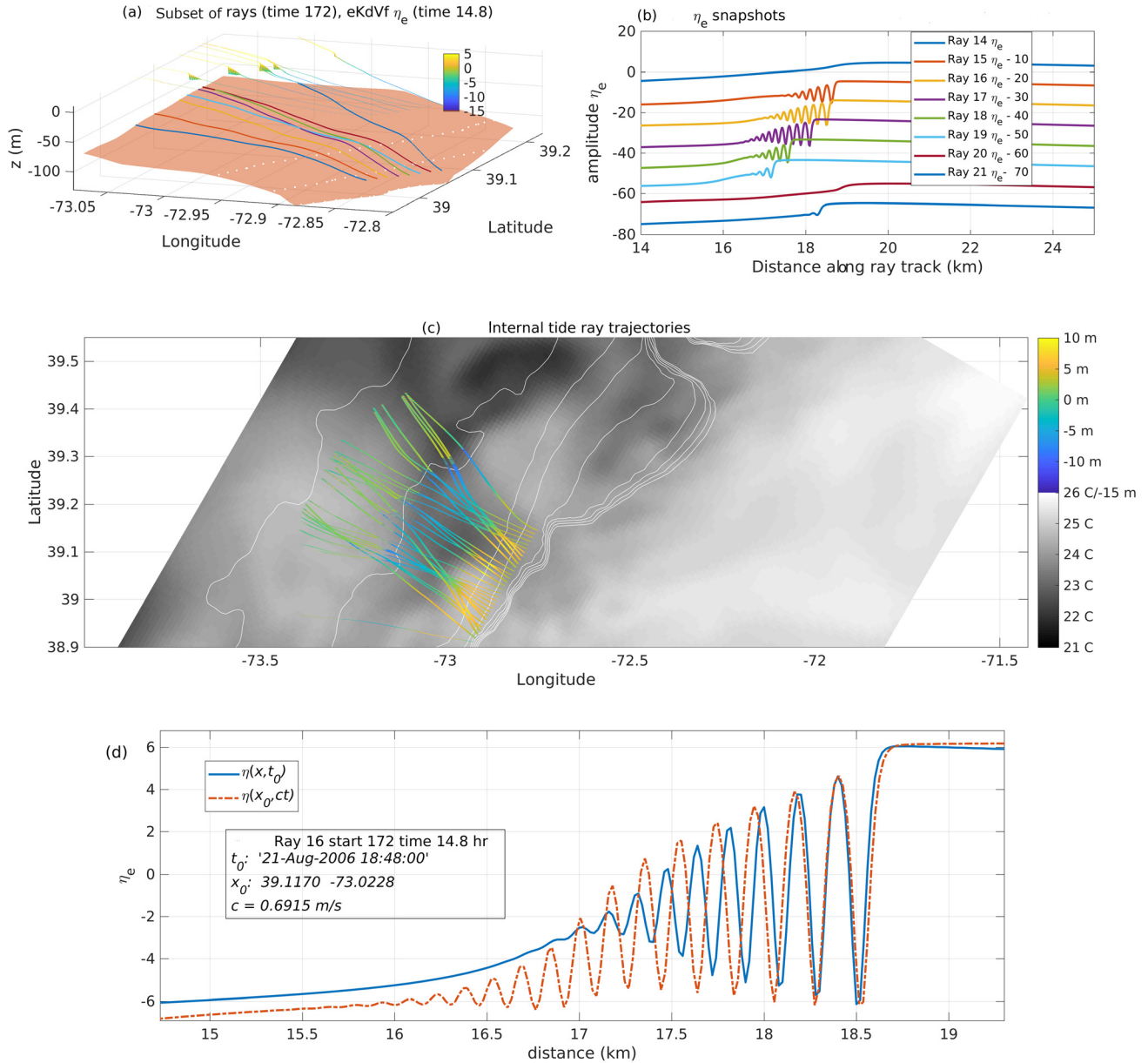


FIG. 9. (Color online) (a) Eight ray trajectories for an MSEAS-based computation are plotted along the bathymetry. The ray colors are indicated in the (b) legend. Bathymetry is contoured in 20 meter intervals. Above each ray, the output of the eKdVf wave model, Eq. (8), is displayed in color (displacement  $\eta_e$  range from  $-15$  to  $5$  m). (b) The mode-one amplitude values  $\eta_e(t, s)$ , barely visible in (a), are shown versus along-ray distance for each of the rays in (a). Short NNIW develop along the central five rays. (c) The entire set of 31 ray trajectories for this simulation are plotted, with color indicating  $\eta_e$  and the grayscale representing surface temperature. (d) Waveforms for ray 16 are shown: an along-trajectory waveform at one time, and a timeseries passing an along-trajectory location, converted to distance using the speed  $c$ .

will cross. In general, rays on the shelf curve much less than they do in deep-water areas with energetic flow such as the Gulf Stream (Duda *et al.*, 2018).

## V. INITIALIZE AND RUN THE EKDVf MODEL

A wave evolution model that includes wave motions with nonhydrostatic pressure as well as the hydrostatic internal tides can be implemented along the internal-tide rays to estimate NNIW behavior. A few models governing internal wave modal evolution are available from the Korteweg-de Vries (KdV) family, with the simplest original KdV equation having no rotation, first-order nonlinear expansion, and applying to plane waves (or cylindrically symmetric modal

waves such as mode-one baroclinic waves or ocean surface waves (Lee and Beardsley, 1974). The equation that is chosen here is the rotationally modified extended Korteweg-de Vries equation (eKdVf, Holloway *et al.*, 1999; Grimshaw, 1985), written

$$\frac{\partial}{\partial s} \left( \frac{\partial \eta}{\partial t} + (c + A_1 \eta + A_2 \eta^2) \frac{\partial \eta}{\partial s} + B \frac{\partial^3 \eta}{\partial s^3} + \frac{c}{2Q} \frac{\partial Q}{\partial s} \eta \right) = G \eta, \quad (8)$$

where  $c$  is linear phase speed of the wave mode being analyzed (baroclinic mode one in our case, thus,  $c_1$ ), and  $\eta(s)$  is the mode amplitude along the path with length increment  $ds$ .

Variable coefficients that depend on the varying density and current profiles are  $A_n$  that appear in the quadratic and cubic nonlinearity terms, the coefficient of nonhydrostatic dispersion  $B$ , and finally  $G$  of the rotational term (equal to  $f^2/2c$  in the absence of a background flow).  $Q$  is an amplification quantity related to conservation of wave action. When the equation is solved, the output for mode  $n$  is labeled  $\eta_n(t, s)$ . Dissipation has been added to the system in a manner similar to that of Liu *et al.* (2004) (but not equivalent) because shelf NNIW have been observed to decay (Sandstrom and Oakey, 1995; Shroyer *et al.*, 2010), and the waves that appear with no drag tend to be larger than observed in nature. The dissipation term takes the form of quadratic drag,  $F = DC_D|\eta|\eta$ , added to Eq. (8), where  $D$  is also a coefficient that depends on the density and current profiles. A feature not yet implemented is a horizontal convergence term to account for amplification of energy by adjacent ray convergence, similar to the  $Q$  term for action conservation under depth changes. Also, note that the quadratic drag applies to the internal waves and does account for any barotropic flows (either tides or mean flows). The drag term is an approximate treatment of all neglected dissipation processes.

Equation (8) is transformed for solution. With change in variable  $W = \eta Q^{1/2}$  and coordinate  $\xi = \int c^{-1}(s)ds - t$  such that  $ds = cd\xi$ , the equation becomes

$$\frac{\partial}{\partial \xi} \left( \frac{\partial W}{\partial s} + \left( \frac{A_1 W}{c^2 Q^{1/2}} + \frac{A_2 \eta^2}{c^2 Q} \right) \frac{\partial W}{\partial \xi} + \frac{B}{c^4} \frac{\partial^3 W}{\partial \xi^3} + \frac{DC_D}{cQ^{1/2}} W|W| \right) = GW. \quad (9)$$

*Coefficients:* These are computed using properties along the track of the internal-wave modes for which Eq. (8) is valid. The equation is valid for modes  $\Phi(z)$  consistent with the long-wave limit eigenvalue equation for vertical displacement

$$\frac{d}{dz} \left\{ [c - U_P(z)]^2 \frac{d\Phi}{dz} \right\} + N^2(z)\Phi = 0, \quad (10)$$

with boundary conditions  $\Phi(0) = \Phi(-H) = 0$ , where  $U_P(z)$  is the background current  $\mathbf{U}(z)$  projected onto the internal-tide ray trajectory (the NNIW direction). Note that Eq. (10) reduces to Eq. (1) when  $\mathbf{U} = 0$ . Note that the modes  $\Phi(z)$  used for NNIW studies along lines differ from the modes  $\hat{w}_n(z)$  used to study internal tidal propagation in two dimensions. The expressions for the coefficients are given in Grimshaw *et al.* (2004); see Alias *et al.* (2014) for  $G$  with background shear. For example

$$A_1 = \left( \frac{3}{2} \right) \frac{\int_{-H}^0 (c - U_P)^2 \left( \frac{d\Phi}{dz} \right)^3 dz}{\int_{-H}^0 (c - U_P) \left( \frac{d\Phi}{dz} \right)^2 dz}. \quad (11)$$

It is evident from the definition that the  $z$  unit vector is directed upward.

*Initial conditions:* Adjusting the mode-one amplitude initial condition  $\eta_I(t, s_0)$  at ray origin  $s_0$  by comparing

against data, such as SW06 experiment data, is critical to obtaining useful results from Eq. (9). The most objective way to initialize the mode-one eKdVf at the  $s_0$  initiation points would be to use mode decomposition to extract the mode-one coefficient from MSEAS-derived  $\eta(x_S, y_S, z, t)$ , either prior to or after a tidal harmonic analysis. However, the extraction of mode-one energy in this way gives small  $\eta_I(t, s_0)$  values that usually give no NNIW formation at locations where NNIW are common in nature, such as the SW06 site. The lack of NNIW is likely because the eKdVf does not allow for mode coupling which must be occurring and strengthening the mode-one amplitude  $\eta_I$  as the mode-one wave move onto the shelf in nature. Essentially, mode coupling must occur at the outer shelf, converting most of the high-mode internal tide energy that is not dissipated to mode-one energy.

The conversion of multi-mode internal tidal beams at the shelf break [beam-like in the vertical; Zhang and Duda (2013)] to the dominantly mode-one internal tides and mode-one NNIW observed on shelves (Rippeth and Inall, 2002) is a process that is not well understood or modeled, so initializing Eq. (8) must be *ad hoc* at this time. Coupled linear equations have been examined (Kelly *et al.*, 2013; Griffiths and Grimshaw, 2007) and weakly nonlinear (Kelly *et al.*, 2016) but not fully nonlinear equations. Taking as the initial condition the displacement time series  $\eta_{IT}(x_S, y_S, t)$  at the depth of maximum displacement variance at the ray origin (Sec. IV C) resulted in NNIW that were unrealistically large. The *ad hoc* method used now is to multiply the tidally-analyzed result  $\eta_{IT}(x_S, y_S, t)$  at the depth of maximum variance [Sec. IV C, Fig. 7(b)] by an attenuation factor and using the result as  $\eta_I(t, s_0)$ . Attenuation factors of from 0.5 to 1 have been used.

Displacement field solutions along rays are plotted in Fig. 9(b). Figure 9(d) also shows a displacement timeseries. Initialization attenuation factor 0.7 and drag coefficient zero are used for this example. These waves compare reasonably with waves measured in this area at the time for which the MSEAS reanalysis regional model simulation was built (Kelly and Lermusiaux, 2016), Fig. 10, although the modeled waves have shorter wavelength. Importantly, the *ad hoc* treatment for the initial conditions, required because KdV-type models do not include the mode coupling energy exchange that is known to occur on the outer shelf, gives uncertainty to the waves amplitudes and the number of waves in the modeled wave packets (or freedom to adjust to match observations).

## VI. BUILD THE 3D SOUND-SPEED FIELD

The mode-one displacement fields with internal tides and NNIW appearing together which are produced by solving the eKdVf along internal tide rays are valid only along the rays, and these assume weak environmental variation normal to the rays. Without regard to whether variation normal to the rays invalidates the eKdVf solutions, we can interpolate features across the gaps between the rays to build 3D sound-speed fields (see ray gaps in Fig. 9). The procedure to build the 3D mode-one NNIW-perturbed sound speed field

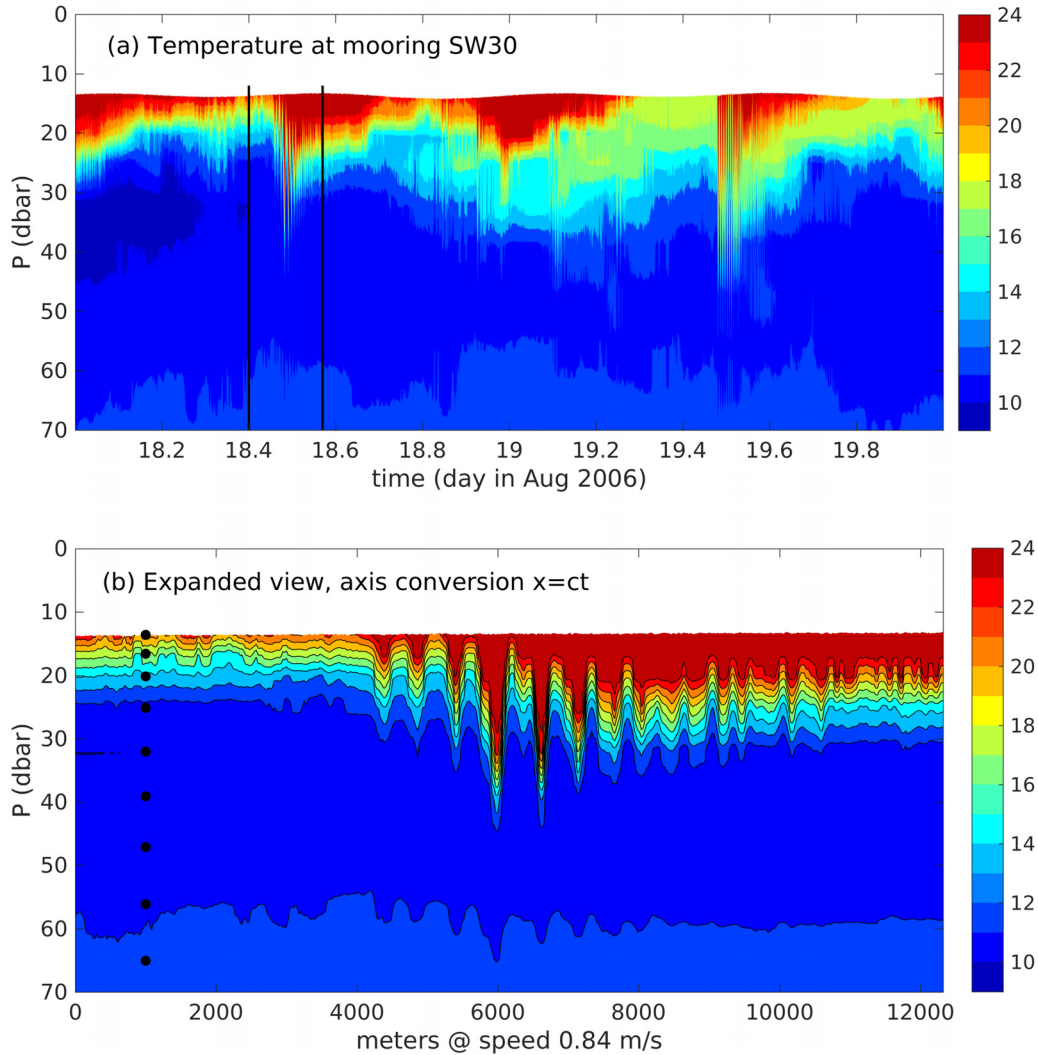


FIG. 10. (Color online) (a) Internal tides and NNIW measured during the SW06 experiment (Newhall *et al.*, 2007) at station SW30, 39° 01.50' N, 73° 04.01' W, are shown. Temperature is contoured versus depth and time. (b) An expanded view of one NNIW group is shown. Time is converted to distance for comparison against eKdVf results; see Fig. 9(d). The nine dots show the instrument depths.

$c_{al}(x, y, z, t)$  is another step where incompatible assumptions in the component models of the system force an *ad hoc* nature onto the procedure.

The primary *ad hoc* treatment of the eKdVf output along rays is an imposed grouping of rays that have similar trajectories, and similar NNIW, that are likely to depict waves in nature that would have connected crests. Chosen groups usually have three to six rays, with the 1-km ray origin spacing used here. Groups may cross, and the waves independently connected. When waves cross, their sum will yield an approximation to the field that disregards the fact that sums of nonlinear waves do not yield the true solution.

Two recipes for interpolation after ray group selection are given here. In the first, a computation of the sound-speed field along the rays  $c_{an}$  from mode- $n$  internal waves is made by first calculating the full-depth displacement field  $\zeta_I(s, z, t) = \eta_I(t, s) \Phi(s, z)$ . The mode-one wave-displaced sound speed field is then computed by remapping,  $c_{al}(s, z + \zeta_I, t) = c_B(s, z, t)$ . If desired, the field can then be interpolated back onto a uniform  $z$ -grid. The field  $c_{al}$  can then be found by interpolation between the internal-tidal lines. Because the NNIW

have long crests that are relatively coherent (Jackson, 2004), a sensible way to do this is to identify a benchmark location for identifiable events at a specific time, such as the location of the leading NNIW in a packet, and fit piecewise cubic ( $x, y$ ) curves through space onto which linear interpolations will be mapped. The method of mapping interpolated fields to a curve is explained in Duda *et al.* (2011).

The second recipe differs by interpolating the mode amplitudes  $\eta_I(s, t)$  onto curves between the lines, then using loosely gridded background conditions to compute  $\zeta_I, c_{al}$ , and  $c_B$  onto a finer grid. The mode-amplitude interpolation method was used in Duda *et al.* (2011) to interpolate into gaps between a line of sensor moorings as NNIW passed by, also for 3D modeling purposes. The interpolation is again best done along curves fitted to (assumed) long-crested NNIW events, as in the previous recipe. With background state known throughout the ( $x, y$ ) plane, and thus the modes, the mode-one displacement can be computed,  $\zeta_I(x, y, z, t) = \eta_I(x, y, t) \Phi(x, y, z)$ , and from this  $c_{al}(x, y, z, t)$  can be computed.

Interpolated two-dimensional (2D)  $\eta_I$  NNIW fields from the family of IODA model runs shown in Figs. 2, 3,

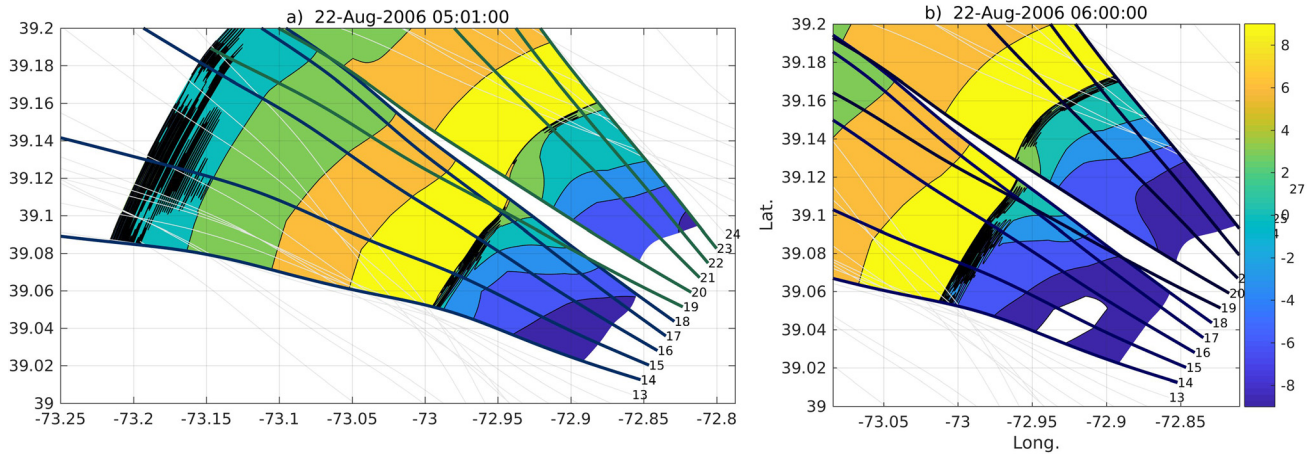


FIG. 11. (Color online) For the MSEAS-based modeling, two interpolated mode-one coefficient fields  $\eta_1$  are shown. (a) This panel shows the UTC time indicated. (b) This panel shows waves 59 min later. In each panel, Interpolations are made for two groups of five  $M_2$  internal tidal rays. The contours are at 3-m increment from  $-9$  m to  $9$  m. One group of rays is shown in black (14–18) in (a) and another is shown in green (19–23). Solitary waves do not appear in Ray 19 so the interpolated NNIW at  $32.1^\circ$  N,  $72.95^\circ$  W do not extend to Ray 20. There is an option to connect them, with protocols to deal with situations like this needing further analysis for successful development.

and 5–9 are shown in Figs. 11 and 12. The second recipe is used. Figure 11 shows two time snapshots of the mode amplitude field, one 59 min after the other, showing the development of NNIW at the north end of the modeled domain in the 59-min time window. The waves move at approximately  $0.75$  m/s so the developing packet has moved about  $3$  km in this time.

## VII. PARABOLIC EQUATION ACOUSTIC SIMULATION

The sound propagation component of the composite model is a time-stepped 3D parabolic equation (PE) simulation method (3.5D method) used by numerous investigators (Oba and Finette, 2002; Finette and Oba, 2003; Heaney and Campbell, 2016). The specific method used in IODA-A is the Cartesian grid 3D split-step Fourier method described in Lin *et al.* (2013a). The code computes the 3D sound field from a harmonic point source embedded in one vertical

boundary wall ( $x=0$ ) of a gridded domain, given by complex pressure coefficient as a function of  $x$ ,  $y$ , and  $z$ , where the  $x$  and  $y$  unit vectors are in the horizontal direction and the  $z$  unit vector is vertical. Broadband results are computed by aggregating the complex pressures from many frequencies in the chosen frequency band. Many studies utilizing this code have been published (Lin *et al.*, 2009; Lynch *et al.*, 2010; Duda *et al.*, 2011; Lin *et al.*, 2013a).

First of all, the compute domain must be selected. This is typically a rectangle within the larger rectangle of internal tidal ray and NNIW modeling. The source location and frequency (or band) are then selected. The 3D time snapshot of water column sound-speed in the domain is taken from the interpolation process explained in Sec. VI. Before the code can operate, some other inputs and parameters must be provided. The marching step length  $\Delta x$  in the solution algorithm is typically one acoustic wavelength, the transverse grid interval  $\Delta y$  is typically one-half wavelength, and the vertical grid interval  $\Delta z$  is typically one-tenth wavelength. Two other parameters are the update rates for the volumetric sound-speed information, and for the bathymetry; these are updated after a specific marching distance in the “zero-angle”  $x$  direction. At larger distance settings, the 3D simulation domain becomes a sequence (in  $x$ ) of ocean strips with  $y$  dependence that is interpolated onto the acoustic grid. An important input field is the water depth in the domain (the bathymetry), which for best results should be on a much finer grid than the grid for the regional dynamical model. US coastal relief model bathymetry (NOAA, 2011), for example, has three-arc-second resolution, about  $92$  meters. Seabed geoacoustic parameters are also needed to describe the layered medium beneath the water. Here, for illustration, a simple sandy type half-space seabed specification is used: sound speed  $1650$  m/s, density  $1500$  kg m $^{-3}$ , sound attenuation  $0.5$  dB/wavelength.

The 3D acoustic simulation in the area with curved internal waves gives results showing complicated acoustic fields that have been seen in similar environments (Duda

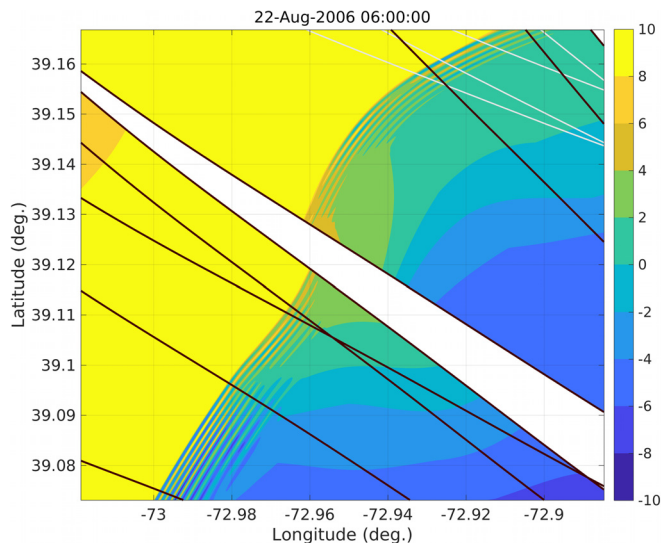


FIG. 12. (Color online) An expanded view of the  $\eta_1(x, y)$  field of Fig. 11(b) is shown.

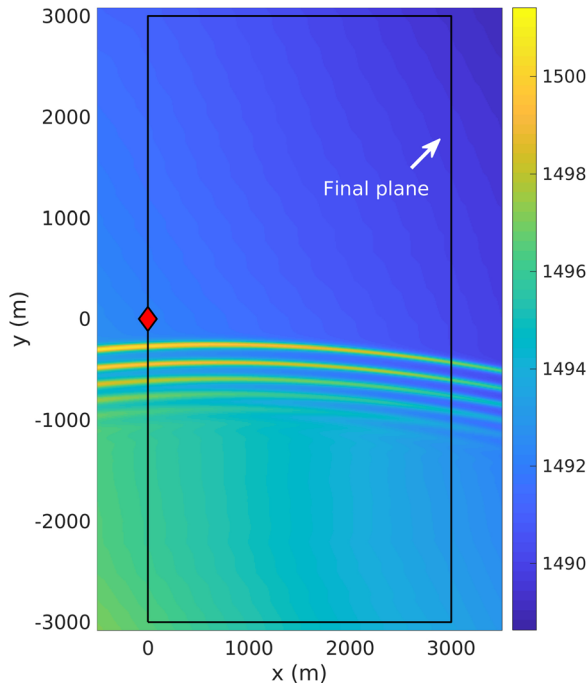


FIG. 13. (Color online) Mid-water column sound speed is shown for an acoustic simulation domain, with the domain boundaries shown with black lines. The waves are from the upper portion of Fig. 12. The acoustic source location at (0,0) is marked. The final plane at  $x = 3006$  m where the results shown in Fig. 14 apply is also marked.

*et al.*, 2011, Lynch *et al.*, 2010). Figure 13 shows the domain for a 500-Hz simulation of 3 km in the area of curved waves in the upper half of Fig. 12, with  $x$  axis directed to the north-east. The source depth is 60 m. Figure 14 shows the waves and the acoustic field level in the final plane at  $x = 3006$  m. The acoustic field inside the NNIW packet, or after transiting the packet, has an entirely different spatial structure than it does away from the packet. This difference, relevant for array signal processing, which can be quantified by either the horizontal acoustic coherence scale or the phase structure function (Duda *et al.*, 2012), is the motivation for this study of NNIW predictability methods.

### VIII. CASE STUDY RESULTS

In this section, the results from two example computations (case studies) are shown. The first case study is idealized in that climatology is used to define the environment, so it is only weakly guided by data. It focuses on the NNIW computation part of the system. The second case study is a full implementation of the system, with the regional model assimilating field data to constrain all downstream aspects of the modeling.

In the first study, the IODA-A model NNIW calculation is tested in the idealized shelf break canyon environment that was discussed in Sec. II. In this situation, the hydrostatic MITgcm canyon model cannot properly model the NNIW that are generated to the right of the canyon. Instead, it produces a smoothed large patch of isopycnal depression at the NNIW location [Fig. 3(a)]. On the contrary, the high-resolution

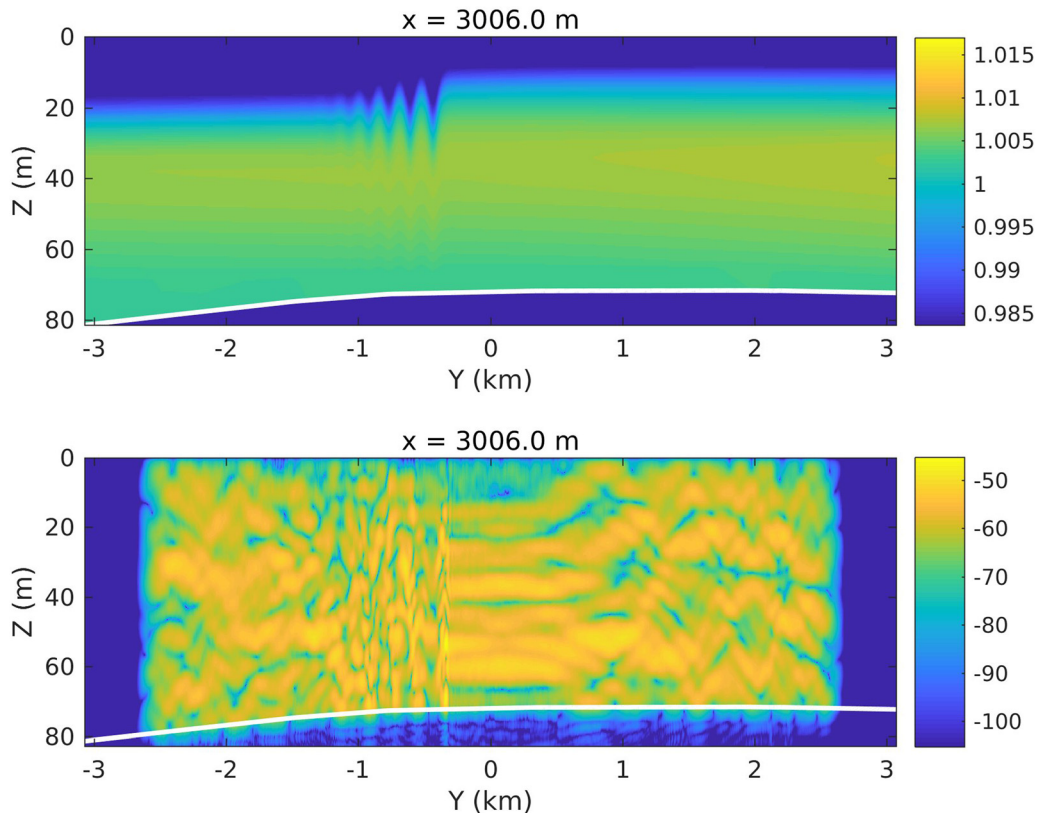


FIG. 14. (Color online) The top panel shows acoustic refractive index in the final plane of one 3D acoustic simulation. The seabed can be seen. The lower panel shows the acoustic field level in the same plane, dB scale.

nonhydrostatic model captures the small-wavelength NNIWs nicely [Fig. 3(b)]. Unfortunately, the high required resolution and the slow pace of the solver make this type of direct real-time nonhydrostatic predictions impossible at this time. With the IODA-A model, the NNIWs in the canyon vicinity can be produced in a timely manner. Figure 15 shows the results obtained using the IODA-A composite model. A concentration of NNIWs are reproduced at approximately the same location as in the nonhydrostatic MITgcm model. Figure 15(a) shows the internal-tide ray initial angles, as well as the highly variable internal-tide displacement amplitudes at the ray origins, depicted by the arrow lengths which are scaled by the rate of energy conversion from surface to internal tides (Zhang *et al.*, 2014). Figure 15(b) shows the eKdVf model output along the rays. NNIW appear to the right of the canyon (facing into shallow water), consistent with the full nonhydrostatic modeling (Fig. 4). Note that some outlier trajectories are initiated on the left side of the canyon where internal tides are weak and difficult to isolate from other flow features.

In the second example, signals arriving at synthetic horizontal arrays in the New Jersey shelf NNIW simulation of Figs. 11 and 12 are examined. This example illustrates how modeling like this has a much different sonar performance prediction capability than modeling such as in Colin *et al.* (2013) would have. That work used an older coarser version of the MSEAS fields than used here and excluded internal tidal bores and NNIW. Figure 16(a) shows the computation domain for a 1000-Hz 3D parabolic equation simulation with source depth 60 m. The variable water depth (between 71 and 77 m) does not strongly affect the acoustic field. Figure 16(b) shows the magnitude of the complex field at 40 m depth, where the NNIWs are clearly seen to interrupt the modal interference pattern that prevails when sound does not encounter NNIWs. The depth-averaged acoustic energy [Fig. 16(c)] shows effects of horizontal refraction in the form of sound focusing by temporary ducting between internal waves, and of shadowing behind the internal waves at  $(x, y)$  near  $(-500, 6200)$ .

Figure 17 shows effects of propagation disruption by the NNIW on array gain examined with array-like horizontal

sampling of the field. In this calculation, fields at arrays of 40 elements at 0.75 m spacing ( $\sim 30$  m length) aligned with the  $y$  axis at 40 m depth are examined for NNIW-induced coherence changes and beamformer array gain degradation. Figure 17(a) shows the coherence length scale, which is the point where the normalized  $y$ -lagged correlation function of the complex field falls to  $\exp(-1)$  from unity at zero lag, or the array length, whichever is smaller. The correlation calculation is made as in Duda *et al.* (2012). Except for a few outliers, the correlation scale away from the NNIW exceeds the 30-m array length (20 wavelengths), but it can drop to as low 4 m (less than three wavelengths) where affected by the NNIW. The physics effects leading to the decorrelation are discussed in Lynch *et al.* (2010) and Duda *et al.* (2011). Figure 17(b) shows array-average single-element acoustic signal excess (SE) at the source in dB, simply  $SE = SL - TL - NL$ , which is a scaled form of transmission loss (TL) equal to sound pressure level at the source (SL) minus TL minus noise level (NL) at the receiver, with SL 130 dB and NL 85 dB chosen to illustrate array performance. 3D propagation effects are seen in SE, as they are in the coherence length. Figure 17(c) shows simulated array performance. Simulated field values are coherently summed with beam-steering in the direction of the source (conventional beamforming), with the plot showing  $SE = SL + AG - TL - NL$ , where AG is the array gain in dB from the summation. Figure 17(d) shows array gain degradation (see caption). The degradation of horizontal array gain within and behind the NNIW is apparent and is quantified. Comparable coherence changes and episodic array gain degradation within internal waves in oceanic experiments have been reported by Orr *et al.* (2004), Collis *et al.* (2008), and Duda *et al.* (2012). Those field measurements of array performance sensitivity to internal wave presence motivated this research into the factors that control internal wave energy and location. The simulations show that degradation can be correlated with NNIW presence.

The variability of AG, diagnosed from the 3D simulations, can be entered into the predictive probability of detection (PPD) framework (Robinson *et al.*, 2002; Lermusiaux

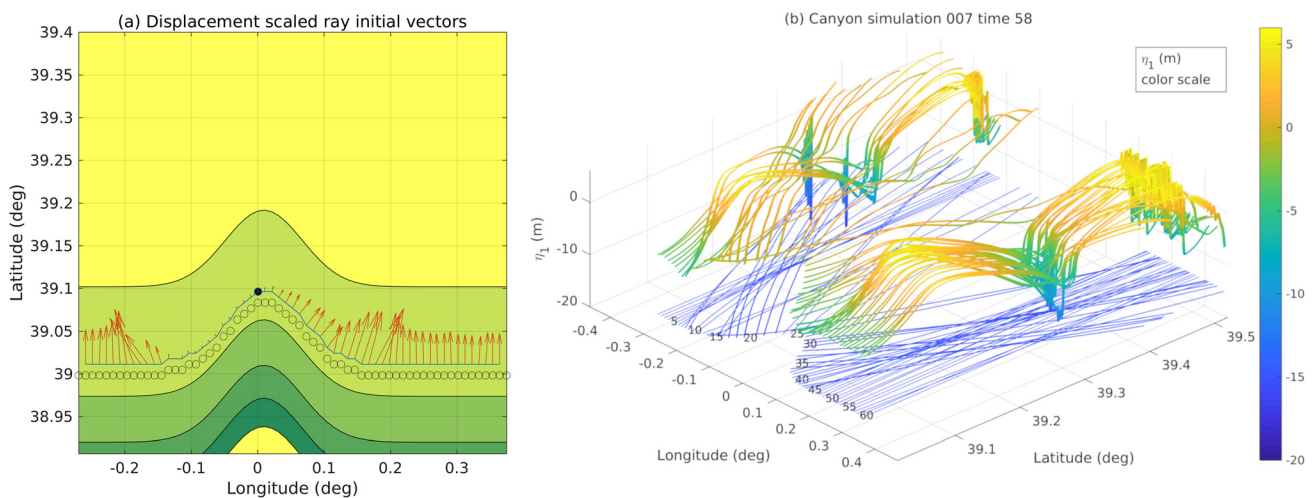


FIG. 15. (Color online) (a) Gaussian canyon simulation ray initialization vectors inshore of the critical slope zone (shown with circles) with length scaled by the eKdVf initialization  $\eta_I(t, s_0)$  rms values. (b) Mode-one displacement amplitudes  $\eta_1$  along the rays (internal tide trajectories; blue lines) are shown for one time snapshot, plotted as  $z$  displacements, in meters.

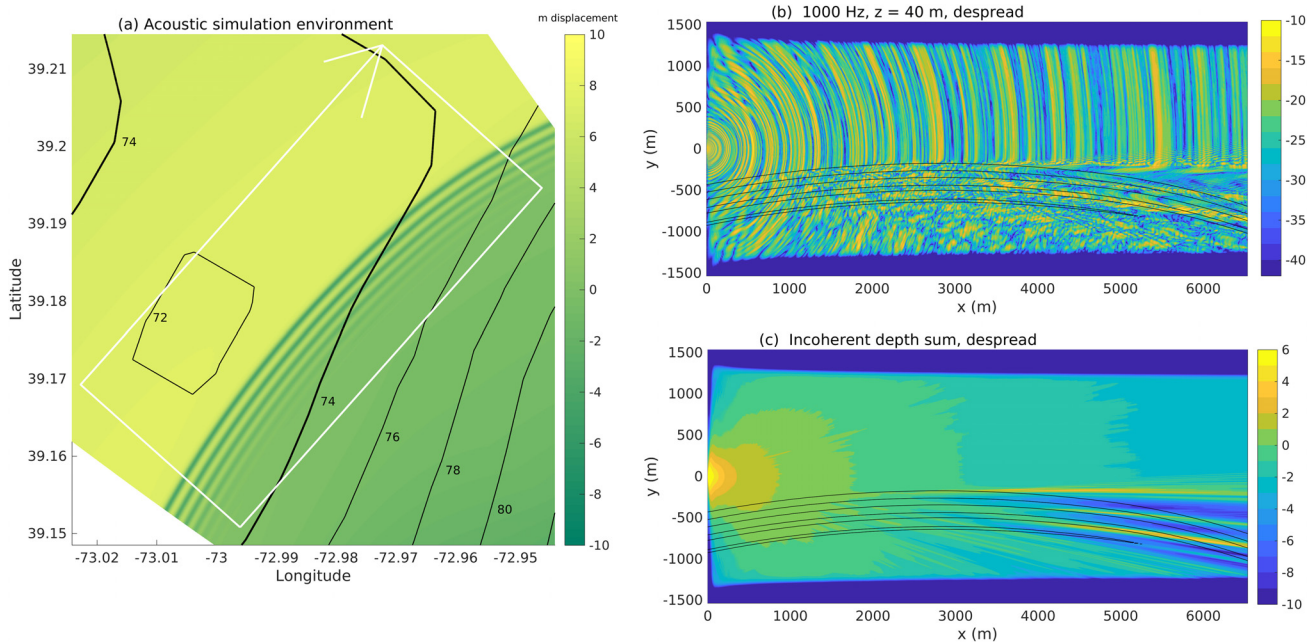


FIG. 16. (Color online) (a) The domain of a 1000-Hz 3D simulation is shown with a box. The source is at the middle of the line marking the southwest edge of the box, with the arrow pointing in the  $x$  direction. The colors show mode-one displacement amplitudes  $\eta_1$  as depicted in Figs. 11(b) and 12. The bathymetry is contoured. (b) This panel shows the acoustic field level (dB re source level) at depth 40 m in the simulation domain of (a). In black, the 1515 m/s contour of the sound speed at 17 m depth marks the internal wave locations. Cylindrical spreading is compensated by multiplying the field by  $r^{1/2}$  where  $r$  is distance from source at  $(x, y) = (0, 0)$ . (c) The incoherent depth-average field strength is plotted, with spreading compensated by multiplying the energy sum by  $r$ .

*et al.*, 2002; Robinson and Lermusiaux, 2004; Emerson *et al.*, 2015). In PPD, the quantities in the sonar equation are treated as random variables with probability distributions so that SE can also be expressed as a probability distribution.

Emerson *et al.* (2015) examine TL and NL distributions in experimental data, with TL variability being near 2 dB rms and appearing lognormal. The AG in our example (Fig. 18) shows similar standard deviations near 2 dB in small areas

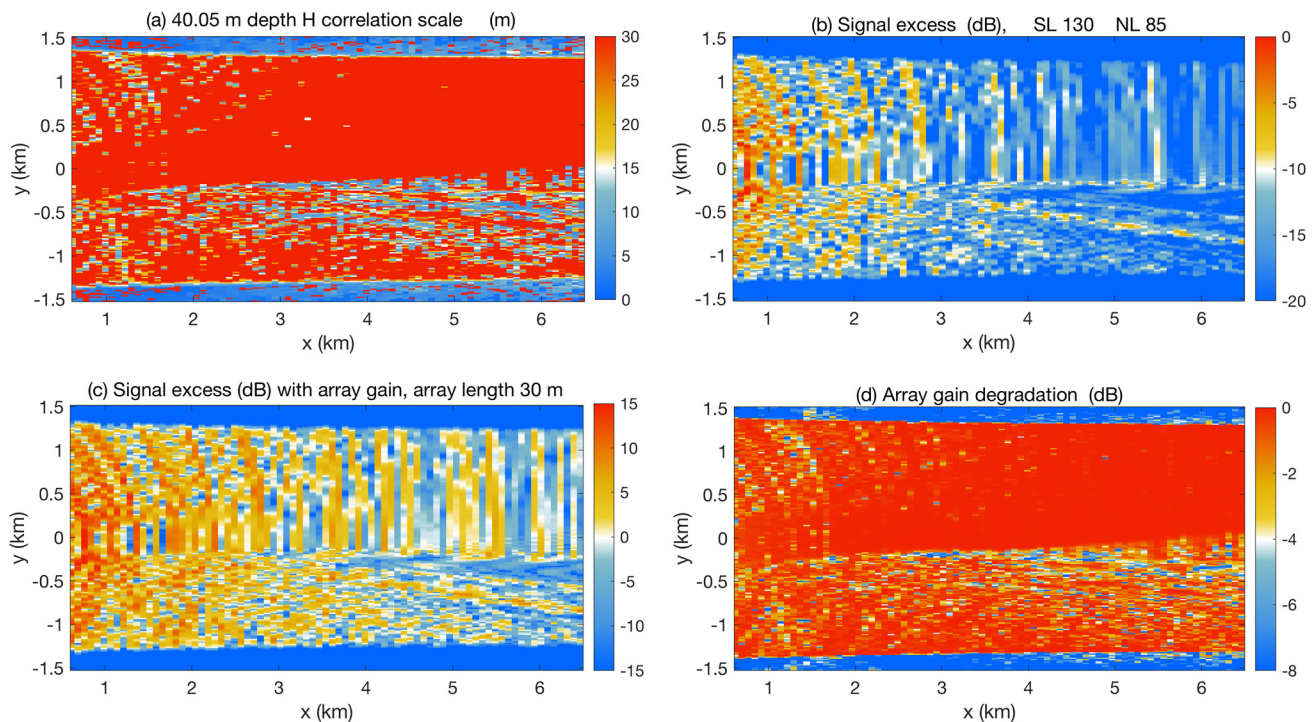


FIG. 17. (Color online) (a) The field coherence length in the  $y$ -direction at 40 m depth is shown, plotted in color at the location of each array center. Arrays of 30-m length are used, so 30 m is the maximum. (b) The average signal excess along each array is plotted (a shifted version of transmission loss), also at each array center, for source level 130 dB, noise level 85 dB. This is below 0 dB except for some locations very close to the source. (c) The signal excess after array gain is applied via coherent summation (plane-wave beamforming, with beam steered toward the source). The areas where this exceeds 0 dB occur with patterns. (d) The array gain degradation is plotted for each array center. This is AG-TG, where TG is the theoretical gain of each 40-element 30-m array,  $10\log(40) = 16$  dB.



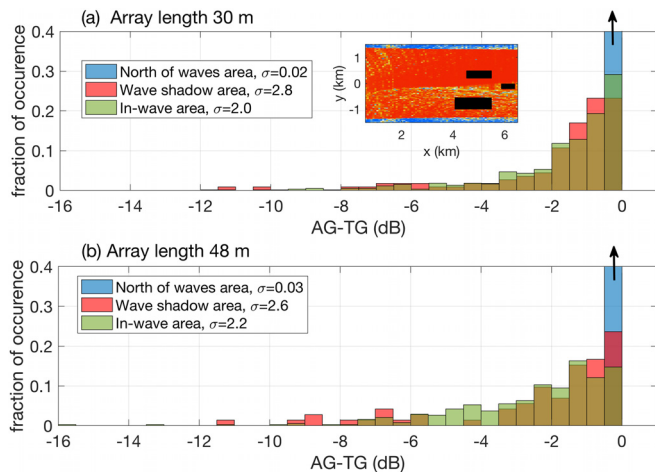


FIG. 18. (Color online) (a) Histograms of the 30-m length array gain degradation AG-TG [Fig. 17(d)] from three small areas of the domain are shown. The inset shows Fig. 17(d) data and the selected areas. An area away from the NNIW has virtually all values between  $-0.5$  and  $0$  dB, with fraction of occurrence one, off the scale. A large area inside the NNIW exhibits large gain large variability, as does a small area in the NNIW shadow. (b) Histograms of the same quantities from the same simulation data are shown except that longer synthetic arrays of 48 m are used.

inside the internal waves and in the area in the shadow of the waves, although the distributions are not lognormal. Including the AG variability in the PPD SE calculations can quantify the increased uncertainty of detection when using array sensors spanning tens of meters in or near NNIW.

## IX. DISCUSSION

The 3D ocean acoustic simulation system presented here builds on many well-developed component models that have been carefully investigated and validated when used individually for the purposes they were designed for. The challenges lie at the interfaces of the models, where physics inconsistencies force the simulation outputs from one modeling element to be adjusted to fit the framework of the interfaced modeling element. A few challenges have been pointed out in Secs. II–VII, and the chosen solutions (many *ad hoc*) were explained. However, much work remains to be done.

The most basic inconsistency at a model interface is the hydrostatic-pressure/nonhydrostatic pressure inconsistency. The regional models are restricted to hydrostatic pressure, by computational necessity, whereas the nonhydrostatic pressure is a key element of tidal bore and NNIW physics. To illustrate the regional model restriction, two simulations with nonhydrostatic pressure were performed using the MITgcm. One had tidally forced flow over an idealized canyon with Gaussian shape and was presented by Duda *et al.* (2016). The simulation required 720 processors operating for four weeks of clock time to simulate six tidal cycles of internal waves. Running a model like this in forecast mode with data assimilation is not plausible because the model pace is so much slower than real time. Thus, the insertion of a KdV-type nonhydrostatic wave model into a domain modeled with a hydrostatic model is likely to persist as a strategy.

This inconsistency means that the regional ocean model output is unreliable for some purposes where significant

nonhydrostatic pressure exists and blending regional model output with KdV-type wave models will give unreliable NNIW output in these areas because the KdV initial conditions will be flawed and unphysical. The practice in our model is to use output only from areas with no steep internal waves (consistent with hydrostatic pressure throughout) as input to the internal-tide raytracing and eKdVf modeling. The outer shelf edge (shelf break) site satisfies this criterion for simulations with MSEAS regional model input examined here, and the outer shelf site satisfies this for Inner-Shelf program wave modeling (not shown here) with data-driven ROMS input.

The separation of internal-tide displacements from the background using isopycnal tracking has difficulties when advection brings new water of new density into the uppermost or lowermost depths. This is more of an operational problem than a physical inconsistency, and only occurs when isotherms are tracked independently by site. A 2D or 3D method of isotherm tracking and time-averaging (to separate waves from evolving background) should be implemented. The methods explained here give reasonable internal-tide initial conditions (Figs. 7, 8, and 15), although the apparent outliers in ray initial direction (Fig. 15) suggest a possible inadequacy under some conditions. The initial conditions provided to the mode-one eKdVf model for NNIW calculation are more challenging, as along-ray radiating energy that does not pass through the tidal harmonic analysis may be essential to include but is difficult to isolate from other time-dependent motions. Effects of coupled-mode internal tide propagation in the ray starting area are not considered. Only near-seabed internal tide (multi-mode) displacements are used, while thermocline-trapped mode-one incident wave displacements (evident in data and models) have not yet been included in the ray and eKdVf modeling.

The results shown here do not include full effects from barotropic tidal currents on the solution, as explained in Sec. III. Instead, these oscillating currents were averaged away in the background state estimate, with a small residual remaining. These currents would serve to advect the entire set of solution fields from Sec. V onward (internal-tide rays, positions of NNIW along rays, 3D sound-speed field). These currents are knowable, and this correction can be made. Note that effects of barotropic tides on internal tide phase, pointed out by Zhang and Duda (2013) are included in the regional model physics, and thus in eKdVf initial condition displacements at ray origins,  $\eta_I(t, s_0)$ .

Another inconsistency appears when internal-tide rays cross, and eKdVf wave simulations cannot be justifiably merged into a single result for the crossing site (Figs. 9, 11, and 15 show crossing rays). The two-dimensional evolution can be studied with the Kadomtsev-Petviashvili (KP) equation (Apel *et al.*, 2007), which has only the first-order nonlinear term and has no rotation, consistent with  $A_2$  and  $f$  equal to zero in Eq. (8). This equation is consistent only with a weakly-refracted beam of waves, as seen in Fig. 9(c). It is notable that internal-tide refraction on the shelf as in Fig. 9(c) results in ray deflections that are generally less than a few degrees after tens of km of propagation. This refraction is much weaker than can occur in extreme cases of strong currents in deep water such as the Gulf Stream (Duda *et al.*, 2018), so this restriction is tolerable. On the other hand, the

importance of the cubic nonlinear term in locations where  $A_1$  (the quadratic nonlinear term coefficient) is zero is well known, and this situation is common on shelves.

Because one of the main objectives of this modeling is to locate NNIW packets for acoustic prediction purposes, and to provide estimates of packet speed, direction, wave height, and quantity of waves, the accuracy of such quantities should be determined using data. The effects of the packets on sound propagation can be strong, as explained in the work cited in the introduction, and the effects can be anisotropic, so knowing NNIW geometries and performing acoustic field predictions may be valuable in some situations. Nonhydrostatic modeling has been shown to give realistic nonlinear internal tides that compare well with data in a setting where bathymetry and tidal flow dominate the response (Rayson *et al.*, 2018), but that effort had horizontal resolution of 100-m or coarser on an unstructured grid, and was not capable of resolving all NNIW. A shortcut approach to the NNIW prediction problem was explored by Min *et al.* (2019) who used nonhydrostatic MITgcm in an idealized way to study their formation in the South China Sea. Despite some uncertainty that must be assigned to our simulation results, our approach can provide objective estimates of NNIW properties in areas where the required supporting information is available.

## X. SUMMARY

We have shown that the modeling and prediction of NNIW can be pursued by a hierarchical composite modeling system. One common feature of the several wave models that make up the system is their restriction to one-way simulated waves. These are, namely, the extended Korteweg-de Vries model, the internal tide ray model, and the acoustic parabolic equation model. The observation of features at sea and analysis of more general (hyperbolic) forms of the governing equations validate the usefulness of the more easily obtained one-way solutions. The fact that the one-way wave methods give usable solutions for actual conditions makes possible the method of multiscale multiphysics ocean acoustic simulation explained here.

Despite the successful modeling to date, it is recognized that each dynamical model in the system has limitations. Together, however, they can reproduce with good reliability:

- (1) Data-informed tidally-forced (sub)-mesoscale regional conditions.
- (2) Tidally driven internal waves (internal tides) in their source region.
- (3) Trajectories of internal tide energy flux.
- (4) Nonlinear nonhydrostatic internal wave formation and propagation.

The volumes within which these processes are simulated using the methods outlined in the paper contain predicted features that are important for 3D acoustic propagation. An ability to simulate the acoustically relevant features like NNIW has been demonstrated. The quality and uncertainty of the NNIW predictions, and thus acoustic propagation predictions, remains to be examined in follow-up work.

## ACKNOWLEDGMENTS

This work was supported by Department of Defense Multidisciplinary University Initiative (MURI) Grant No. N00014-11-1-0701, managed by the Office of Naval Research Ocean Acoustics Program, and National Science Foundation Grant No. OCE-1060430. Final manuscript preparation was supported by ONR Ocean Acoustics Grant Nos. N00014-17-1-2624 and N00014-17-1-2692. P.F.J.L. also thanks ONR and NSF for research support under Grant Nos. N00014-13-1-0518 (Multi-DA) and OCE-1061160 (ShelfIT) to MIT, respectively. The MSEAS-based series of simulations for the New Jersey shelf region examined here was accelerated toward completion by the interest in realistic 3D acoustic fields expressed by Dr. Ivars Kirsteins at the Naval Undersea Warfare Center.

- Alias, A., Grimshaw, R., and Khusnutdinova, K. (2014). "Coupled Ostrovsky equations for internal waves in a shear flow," *Phys. Fluids* **26**, 126603.
- Apel, J. R., Ostrovsky, L. A., Stepanyants, Y. A., and Lynch, J. F. (2007). "Internal solitons in the ocean and their effect on underwater sound," *J. Acoust. Soc. Am.* **121**, 695–722.
- Arbic, B. K., Wallcraft, A. J., and Metzger, E. J. (2010). "Concurrent simulation of the eddying general circulation and tides in a global ocean model," *Ocean Model.* **32**, 175–187.
- Badiev, M., Katsnelson, B. G., Lynch, J. F., Pereselkov, S., and Siegmann, W. L. (2005). "Measurement and modeling of three-dimensional sound intensity variations due to shallow-water internal waves," *J. Acoust. Soc. Am.* **117**, 613–625.
- Bleck, R. (2002). "An oceanic general circulation model framed in hybrid isopycnal Cartesian coordinates," *Ocean Model.* **4**, 55–88.
- Carter, G. S., Merrifield, M. A., Becker, J. M., Katsumata, K., Gregg, M. C., Luther, D. S., Levine, M. D., Boyd, T. J., and Firing, Y. L. (2008). "Energetics of M2 barotropic-to-baroclinic tidal conversion at the Hawaiian Islands," *J. Phys. Oceanogr.* **38**, 2205–2223.
- Colin, M. E. G. D., Duda, T. F., te Raa, L. A., van Zon, T., Haley, P. J., Jr., Lermusiaux, P. F. J., Leslie, W. G., Mirabito, C., Lam, F. P. A., Newhall, A. E., Lin, Y.-T., and Lynch, J. F. (2013). "Time-evolving acoustic propagation modeling in a complex ocean environment," in *Oceans '13 Bergen Conference Proceedings*, June 10–13, Bergen, Norway.
- Collis, J. M., Duda, T. F., Lynch, J. F., and DeFerrari, H. A. (2008). "Observed limiting cases of horizontal field coherence and array performance in a time-varying internal wavefield," *J. Acoust. Soc. Am.* **124**, EL97–EL103.
- Duda, T. F. (2004). "Acoustic mode coupling by nonlinear internal wave packets in a shelfbreak from area," *IEEE J. Oceanic Eng.* **29**(1), 118–125.
- Duda, T. F., Collis, J. M., Lin, Y.-T., Newhall, A. E., Lynch, J. F., and DeFerrari, H. A. (2012). "Horizontal coherence of low-frequency fixed-path sound in a continental shelf region with internal-wave activity," *J. Acoust. Soc. Am.* **131**, 1782–1797.
- Duda, T. F., Lin, Y.-T., Buijsman, M., and Newhall, A. E. (2018). "Internal tidal modal ray refraction and energy ducting in baroclinic Gulf Stream currents," *J. Phys. Oceanogr.* **48**, 1969–1993.
- Duda, T. F., Lin, Y.-T., Newhall, A. E., Helffrich, K. R., Zhang, W. G., Badiev, M., Lermusiaux, P. F. J., Colosi, J. A., and Lynch, J. F. (2014a). "The 'Integrated Ocean Dynamics and Acoustics' (IODA) hybrid modeling effort," in *Proceedings of the 2nd Underwater Acoustics Conference and Exhibition*, June 22–27, Rhodes, Greece, pp. 621–628.
- Duda, T. F., Lin, Y.-T., and Reeder, D. B. (2011). "Observationally constrained modeling of sound in curved ocean internal waves: Examination of deep ducting and surface ducting at short range," *J. Acoust. Soc. Am.* **130**, 1173–1187.
- Duda, T. F., and Preisig, J. C. (1999). "A modeling study of acoustic propagation through moving shallow-water solitary wave packets," *IEEE J. Oceanic Eng.* **24**, 16–32.
- Duda, T. F., and Rainville, L. (2008). "Diurnal and semidiurnal tide energy flux at a continental slope in the South China Sea," *J. Geophys. Res. Oceans* **113**(C3), C03025, <https://doi.org/10.1029/2007JC004418>.

- Duda, T. F., Zhang, W. G., Helfrich, K. R., Lin, Y.-T., and Newhall, A. E. (2016). "Modeling internal solitary wave development at the head of a submarine canyon," in *Proceedings of the 8th International Symposium on Stratified Flows (ISSF)*, August 29–September 1, San Diego, CA, available at <https://escholarship.org/uc/item/2xm7j16t>.
- Duda, T. F., Zhang, W. G., Helfrich, K. R., Newhall, A. E., Lin, Y.-T., Lynch, J. F., Lermusiaux, P. F. J., Haley, P. J., Jr., and Wilkin, J. (2014b). "Issues and progress in the prediction of ocean submesoscale features and internal waves," in *Oceans '14 St. John's Conference Proceedings*, September 14–19, St. John's, Canada.
- Edwards, C. A., Moore, A. M., Hoteit, I., and Cornuelle, B. D. (2015). "Regional ocean data assimilation," *Ann. Rev. Mar. Sci.* **7**, 21–42.
- Emerson, C., Lynch, J. F., Abbot, P., Lin, Y.-T., Duda, T. F., Gawarkiewicz, G. G., and Chen, C.-F. (2015). "Acoustic propagation uncertainty and probabilistic prediction of sonar system performance in the southern East China Sea continental shelf and shelfbreak environments," *IEEE J. Oceanic Eng.* **40**, 1003–1017.
- Finette, S., and Oba, R. (2003). "Horizontal array beamforming in an azimuthally anisotropic internal wave field," *J. Acoust. Soc. Am.* **114**, 131–144.
- Gerkema, T., Lam, F.-P. A., and Maas, L. R. M. (2004). "Internal tides in the Bay of Biscay: Conversion rates and seasonal effects," *Deep Sea Res. II* **51**, 2995–3008.
- Griffiths, S. D., and Grimshaw, R. H. J. (2007). "Internal tide generation at the continental shelf modeled using a modal decomposition: Two-dimensional results," *J. Phys. Oceanogr.* **37**, 428–451.
- Grimshaw, R. (1985). "Evolution equations for weakly nonlinear, long internal waves in a rotating fluid," *Stud. Appl. Math.* **73**, 1–33.
- Grimshaw, R., Pelinovsky, E., Talipova, T., and Kurkin, A. (2004). "Simulation of the transformation of internal solitary waves on oceanic shelves," *J. Phys. Oceanogr.* **34**, 2774–2791.
- Haley, P. J., Jr., Agarwal, A., and Lermusiaux, P. F. J. (2015). "Optimizing velocities and transports for complex coastal regions and archipelagos," *Ocean Model.* **89**, 1–28.
- Haley, P. J., Jr., and Lermusiaux, P. F. J. (2010). "Multiscale two-way embedding schemes for free-surface primitive-equations in the Multidisciplinary Simulation, Estimation and Assimilation System," *Ocean Dyn.* **60**, 1497–1537.
- Hall, R. A., Huthnance, J. M., and Williams, R. G. (2013). "Internal wave reflection on shelf slopes with depth-varying stratification," *J. Phys. Oceanogr.* **43**, 248–258.
- Heaney, K. D., and Campbell, R. L. (2016). "Three-dimensional parabolic equation modeling of mesoscale eddy deflection," *J. Acoust. Soc. Am.* **139**, 918–926.
- Holloway, P. E., Pelinovsky, E., and Talipova, T. (1999). "A generalized Korteweg-de Vries model of internal tide transformation in the coastal zone," *J. Geophys. Res. Oceans* **104**(C8), 18333–18350, <https://doi.org/10.1029/1999JC900144>.
- Jackson, C. R. (2004). *An Atlas of Internal Solitary-Like Waves and Their Properties*, 2nd ed. (Global Ocean Associates, Alexandria, VA).
- Jensen, F. B., Kuperman, W. A., Porter, M. B., and Schmidt, H. (2011). *Computational Ocean Acoustics*, 2nd ed. (Springer, New York).
- Jones, W. L. (1967). "Propagation of internal gravity waves in fluids with shear flow and rotation," *J. Fluid Mech.* **30**(3), 439–448.
- Katsnelson, B. G., and Peresl'kov, S. A. (2000). "Low-frequency horizontal acoustic refraction caused by internal wave solitons in a shallow sea," *Acoust. Phys.* **46**, 684–691.
- Kelly, S. M., Jones, N. L., and Nash, J. D. (2013). "A coupled model for Laplace's tidal equations in a fluid with one horizontal dimension and variable depth," *J. Phys. Oceanogr.* **43**, 1780–1797.
- Kelly, S. M., and Lermusiaux, P. F. J. (2016). "Internal-tide interactions with the Gulf Stream and Middle Atlantic Bight shelfbreak front," *J. Geophys. Res.* **121**, 6271–6294, <https://doi.org/10.1002/2016JC011639>.
- Kelly, S. M., Lermusiaux, P. F. J., Duda, T. F., and Haley, P. J., Jr. (2016). "A coupled-mode shallow water model for tidal analysis: Internal-tide reflection and refraction by the Gulf Stream," *J. Phys. Oceanogr.* **46**, 3661–3679.
- Kelly, S. M., Nash, J. D., and Kunze E. (2010). "Internal-tide energy over topography," *J. Geophys. Res.* **115**, C06014, <https://doi.org/10.1029/2009JC005618>.
- Lam, F. P., Haley, P. J., Jr., Janmaat, J., Lermusiaux, P. F. J., Leslie, W. G., and Schouten, M. W. (2009). "At-sea real-time coupled four-dimensional oceanographic and acoustic forecasts during battlespace preparation 2007," *J. Mar. Syst.* **78**, S306–S320.
- Lee, C.-Y., and Beardsley, R. C. (1974). "The generation of long nonlinear internal waves in a weakly stratified shear flow," *J. Geophys. Res.* **79**(3), 453–462, <https://doi.org/10.1029/JC079i003p00453>.
- Lermusiaux, P. F. J. (2006). "Uncertainty estimation and prediction for interdisciplinary ocean dynamics," *J. Comput. Phys.* **217**, 176–199.
- Lermusiaux, P. F. J., Chiu, C.-S., and Robinson, A. R. (2002). "Modeling uncertainties in the prediction of the acoustic wavefield in a shelfbreak environment," in *Proceedings of the 5th International Conference on Theoretical and Computational Acoustics*, May 21–25, Beijing, China, pp. 191–200.
- Lermusiaux, P. F. J., Malanotte-Rizzoli, P., Stammer, D., Carton, J., Cummings, J., and Moore, A. M. (2006). "Progress and prospects of U.S. data assimilation in ocean research," *Oceanography* **19**, 172–183.
- Lermusiaux, P. F. J., Xu, J., Chen, C. F., Jan, S., Chiu, L. Y., and Yang, Y.-J. (2010). "Coupled ocean-acoustic prediction of transmission loss in a continental shelfbreak region: Predictive skill, uncertainty quantification and dynamical sensitivities," *IEEE J. Oceanic Eng.* **35**(4) 895–916.
- Lin, Y.-T., Duda, T. F., and Lynch, J. F. (2009). "Acoustic mode radiation from the termination of a truncated nonlinear internal gravity wave duct in a shallow ocean area," *J. Acoust. Soc. Am.* **126**, 1752–1765.
- Lin, Y.-T., Duda, T. F., and Newhall, A. E. (2013a). "Three-dimensional sound propagation models using the parabolic-equation approximation and the split-step Fourier method," *J. Comput. Acoust.* **21**, 1250018.
- Lin, Y.-T., McMahon, K. G., Lynch, J. F., and Siegmann, W. L. (2013b). "Horizontal ducting of sound by curved nonlinear internal gravity waves in the continental shelf areas," *J. Acoust. Soc. Am.* **133**, 37–49.
- Liu, A. K., Ramp, S. R., Zhao, Y., and Tang, T. Y. (2004). "A case study of internal solitary wave propagation during ASIAEX 2001," *IEEE J. Oceanic Eng.* **29**(4), 1144–1156.
- Logutov, O. G., and Lermusiaux, P. F. J. (2008). "Inverse barotropic tidal estimation for regional ocean applications," *Ocean Model.* **25**, 17–34.
- Lynch, J. F., Lin, Y.-T., Duda, T. F., and Newhall, A. E. (2010). "Acoustic ducting, reflection, refraction, and dispersion by curved nonlinear internal waves in shallow water," *IEEE J. Oceanic Eng.* **35**, 12–27.
- Marshall, J., Hill, C., Perelman, L., and Adcroft, A. (1997). "Hydrostatic, quasi-hydrostatic, and non-hydrostatic ocean modeling," *J. Geophys. Res.* **102**, 5733–5752, <https://doi.org/10.1029/96JC02776>.
- Min, W., Li, Q., Zhang, P., Xu, Z., and Yin, B. (2019). "Generation and evolution of internal solitary waves in the southern Taiwan Strait," *Geophys. Astrophys. Fluid Dyn.* **113**, 287–302.
- Moore, A. M., Arango, H. G., Broquet, G., Edwards, C., Veneziani, M., Powell, B., Foley, D., Doyle, J. D., Costa, D., and Robinson, P. (2011). "The Regional Ocean Modeling System (ROMS) 4-dimensional variational data assimilation systems: II—Performance and application to the California Current system," *Progr. Oceanogr.* **91**, 50–73.
- Moore, A. M., Martin, M., Akella, S., Arango, H., Balmaseda, M., Bertino, L., Ciavatta, S., Cornuelle, B., Cummings, J., Frolov, S., Lermusiaux, P., Oddo, P., Oke, P. R., Storto, A., Teruzzi, A., Vidard, A., and Weaver, A. T. (2019). "Synthesis of ocean observations using data assimilation for operational, real-time and reanalysis systems: A more complete picture of the state of the ocean," *Front. Mar. Sci.* **6**(90), 1–6.
- Newhall, A. E., Duda, T. F., von der Heydt, K., Irish, J. D., Kemp, J. N., Lerner, S. A., Liberatore, S. P., Lin, Y.-T., Lynch, J. F., Maffei, A. R., Morozov, A. K., Shmelev, A., Sellers, C. J., and Witzell, W. E. (2007). "Acoustic and oceanographic observations and configuration information for the WHOI moorings from the SW06 experiment," Tech Report No. WHOI-2007-04, Woods Hole Oceanographic Institution, Woods Hole, MA, available at <https://hdl.handle.net/1912/1826>.
- NOAA National Centers for Environmental Information (2011). "U.S. Coastal Relief Model," <http://www.ngdc.noaa.gov/mgg/coastal/crm.html> (Last viewed 9 September 2019).
- Oba, R., and Finette, S. (2002). "Acoustic propagation through anisotropic internal wave fields: Transmission loss, cross-range coherence, and horizontal refraction," *J. Acoust. Soc. Am.* **111**, 769–784.
- Orr, M. H., Pasewark, B. H., Wolf, S. N., Lynch, J. F., Schroeder, T., and Chiu, C.-S. (2004). "South China Sea internal tide/internal waves – Impact on the temporal variability of horizontal array gain at 276 Hz," *IEEE J. Oceanic Eng.* **29**, 1292–1307.
- Pawlowicz, R., Beardsley, R., and Lentz, S. (2002). "Classical tidal harmonic analysis including error estimates in MATLAB using T\_TIDE," *Comput. Geosci.* **28**, 929–937.
- Ponte, A. L., and Cornuelle, B. D. (2013). "Coastal numerical modelling of tides: Sensitivity to domain size and remotely generated internal tide," *Ocean Model.* **62**, 17–26.

- Preisig, J. C., and Duda, T. F. (1997). "Coupled acoustic mode propagation through continental shelf internal solitary waves," *IEEE J. Oceanic Eng.* **22**, 256–269.
- Raghukumar, K., and Colosi, J. A. (2014a). "High frequency normal mode statistics in a shallow water waveguide: The effect of random linear internal waves," *J. Acoust. Soc. Am.* **136**, 66–79.
- Raghukumar, K., and Colosi, J. A. (2014b). "High frequency normal mode statistics in shallow water: The combined effect of random surface and internal waves," *J. Acoust. Soc. Am.* **137**, 2950–2961.
- Rayson, M. D., Ivey, G. N., Jones, N. L., and Fringer, O. B. (2018). "Resolving high-frequency internal waves generated at an isolated coral atoll using an unstructured grid ocean model," *Ocean Model.* **122**, 67–84.
- Rippeth, T. P., and Inall, M. E. (2002). "Observations of the internal tide and associated mixing across the Malin Shelf," *J. Geophys. Res.* **107**(C4), 3028–3041, <https://doi.org/10.1029/2000JC000761>.
- Robinson, A. R., Abbot, P., Lermusiaux, P. F. J., and Dillman, L. (2002). "Transfer of uncertainties through physical-acoustical-sonar end-to-end systems: A conceptual basis," in *Impact of Littoral Environmental Variability of Acoustic Predictions and Sonar Performance* (Springer, Dordrecht, the Netherlands), pp. 603–610.
- Robinson, A. R., and Lermusiaux, P. F. J. (2004). "Prediction systems with data assimilation for coupled ocean science and ocean acoustics," in *Proceedings of the Sixth International Conference on Theoretical and Computational Acoustics*, August 11–15, 2003, Honolulu, HI (World Scientific, Singapore), pp. 325–342.
- Robinson, A. R., Lermusiaux, P. F. J., and Sloan, III, N. Q. (1998). "Data assimilation," in *The Sea, Ideas and Observations on Progress in the Study of the Seas* (John Wiley and Sons, New York), pp. 541–549.
- Sandstrom, H., and Oakey, N. S. (1995). "Dissipation in internal tides and solitary waves," *J. Phys. Oceanogr.* **25**, 604–614.
- Shchepetkin, A. F., and McWilliams, J. C. (2005). "The Regional Oceanic Modeling System (ROMS): A split-explicit, freesurface, topography-following-coordinate oceanic model," *Ocean Modell.* **9**, 347–404.
- Shmelev, A. A., Lynch, J. F., Lin, Y.-T., and Schmidt, H. (2014). "Three dimensional coupled mode analysis of internal wave acoustic ducts," *J. Acoust. Soc. Am.* **135**(5), 2497–2512.
- Shroyer, E. L., Moum, J. N., and Nash, J. D. (2010). "Energy transformations and dissipation of nonlinear internal waves over New Jersey's continental shelf," *Nonlinear Process. Geophys.* **17**, 345–360.
- Siderius, M., and Porter, M. B. (2008). "Modeling broadband ocean acoustic transmissions with time-varying sea surfaces," *J. Acoust. Soc. Am.* **124**(1), 137–150.
- Suanda, S. H., Feddersen, F., and Kumar, N. (2017). "The effect of barotropic and baroclinic tides on coastal stratification and mixing," *J. Geophys. Res.* **122**(12), 10156–10173, <https://doi.org/10.1002/2017JC013379>.
- Venayagamoorthy, S. K., and Fringer, O. B. (2006). "Numerical simulations of the interaction of internal waves with a shelf break," *Phys. Fluids* **18**(7), 076603.
- Wilkin, J., Zhang, W. G., Cahill, B., and Chant R. C. (2011). "Integrating coastal models and observations for studies of ocean dynamics, observing systems and forecasting," in *Operational Oceanography in the 21st Century*, edited by A. Schiller and G. Brassington (Springer, New York), pp. 487–512.
- Xu, J., Lermusiaux, P. F. J., Haley, P. J., Jr., Leslie, W. G., and Logutov, O. G. (2008). "Spatial and temporal variations in acoustic propagation during the PLUSNet'07 exercise in Dabob Bay," *Proc. Mtgs. Acoust.* **4**, 070001.
- Zhang, W. G., and Duda, T. F. (2013). "Intrinsic nonlinearity and spectral structure of internal tides at an idealized Mid-Atlantic Bight shelf break," *J. Phys. Oceanogr.* **43**, 2641–2660.
- Zhang, W. G., Duda, T. F., and Udovychchenkov, I. A. (2014). "Modeling and analysis of internal-tide generation and beamlike onshore propagation in the vicinity of shelfbreak canyons," *J. Phys. Oceanogr.* **44**, 834–849.
- Zhang, H. P., King, B., and Swinney, H. L. (2008). "Resonant generation of internal waves on a model continental slope," *Phys. Rev. Lett.* **100**, 244504.
- Zhou, J., Zhang, X., and Rogers, P. H. (1991). "Resonant interaction of sound wave with internal solitons in the coastal zone," *J. Acoust. Soc. Am.* **90**, 2042–2054.